Genetically defined nucleus incertus neurons differ in connectivity and function

Emma D. Spikol,[1,2] Ji Cheng,[2,3] Michelle Macurak,[3] Abhignya Subedi,[3] and *Marnie E. Halpern[1,2,3]

[1] Department of Neuroscience, Johns Hopkins University School of Medicine, Baltimore, MD 21205, USA

[2] Department of Molecular and Systems Biology, Geisel School of Medicine at Dartmouth, Hanover, NH 03755, USA

[3] Department of Biology, Johns Hopkins University, Baltimore, MD 21218 USA

Author contributions: EDS and MEH designed research; EDS and AS performed research, EDS, JC, and MM generated tools, EDS analyzed data, EDS and MEH wrote the manuscript.

Corresponding author:
Dr. Marnie E. Halpern
704 Remsen Building
Hanover, NH 03755
Marnie.E.Halpern@dartmouth.edu

Conflict of Interest

The authors declare no competing financial interests.

Abstract

The nucleus incertus (NI), a conserved hindbrain structure implicated in the stress response, arousal, and memory, is a major site for production of the neuropeptide relaxin-3. On the basis of *goosecoid homeobox 2* (*gsc2*) expression, we identified a neuronal cluster that lies adjacent to *relaxin 3a* (*rln3a*) neurons in the zebrafish analogue of the NI. To delineate the characteristics of the *gsc2* and *rln3a* NI neurons, we used CRISPR/Cas9 targeted integration to drive gene expression specifically in each neuronal group, and found that they differ in their efferent and afferent connectivity, spontaneous activity, and functional properties. *gsc2* and *rln3a* NI neurons have widely divergent projection patterns and innervate distinct subregions of the midbrain interpeduncular nucleus (IPN). Whereas *gsc2* neurons are activated by electric shock, *rln3a* neurons exhibit spontaneous fluctuations in calcium signaling and regulate locomotor activity. Our findings define heterogeneous neurons in the NI and provide new tools to probe its diverse functions.

Introduction

The nucleus incertus (NI), originally identified in the human brain (Streeter, 1903), consists of bilaterally paired clusters of neurons at the midline of the floor of the fourth ventricle (Olucha-Bordonau et al., 2018, Ma and Gundlach, 2015). A variety of neuropeptides have been detected in the region, including cholecystokinin (Olucha-Bordonau et al., 2003), neuromedin B (Lu et al., 2020), neurotensin (Jennes et al., 1982), and relaxin-3 (Burazin et al., 2002, Smith et al., 2010), however, the properties of NI neuronal subtypes are not well defined.

Initial investigations in rodents indicate that the NI responds to stressful cues; NI neurons are enriched in receptors for the Corticotropin Releasing Factor (CRF) and upregulate c-Fos in response to CRF exposure (Potter et al., 1994, Bittencourt and Sawchenko, 2000). Placement in an elevated plus maze, exposure to an anxiogenic drug, foot shock, or water-restraint stress also induce expression of the neural activity marker c-Fos in the NI (Lawther et al., 2015, Passerin et al., 2000, Rajkumar et al., 2016). Other reports have implicated the NI in regulating baseline locomotor activity. For example, electrical microstimulation of the NI promotes locomotion in rats (Farooq et al., 2016), and optogenetic activation of a subset of neurons in the mouse NI that produce the neuropeptide neuromedin B increases locomotor speed (Lu et al., 2020).

In rodents, the NI contains the largest population of neurons in the brain that produce relaxin-3 (RLN3) (Tanaka et al., 2005, Smith et al., 2011), a neuropeptide thought to mediate behavioral responses to aversive stimuli (Lawther et al., 2015, Ryan et al., 2013, Zhang et al., 2015). Although there are also NI neurons that do not produce

RLN3 (Ma et al., 2013), their characteristics are not well distinguished from the RLN3 population.

Larval zebrafish are a powerful model to investigate neuronal diversity and connectivity because their transparency and genetic tractability are advantageous for monitoring and manipulating specific subpopulations. In zebrafish, the presumed analogue of the NI is the griseum centrale, situated on the ventral surface of the rhombencephalic ventricle (Wullimann et al., 1996, Agetsuma et al., 2010, Olson et al., 2017). Expression of *relaxin 3a* (*rln3a*) is restricted to two bilaterally paired clusters of neurons in the midbrain and two bilaterally paired nuclei bordering the hindbrain midline (Donizetti et al., 2008). It was proposed that the midbrain *rln3a* expression domains correspond to the periaqueductal grey (PAG), a region that produces RLN3 in rodents (Smith et al., 2010, Tanaka et al., 2005, Ma et al., 2017), and that the hindbrain *rln3a* neuron clusters correspond to the NI (Donizetti et al., 2008).

The zebrafish griseum centrale is a proposed target of the habenulo-interpeduncular nucleus (Hb-IPN) axis, a highly conserved forebrain to midbrain pathway implicated in modulating anxiety and the response to aversive stimuli (Agetsuma et al., 2010, Facchin et al., 2015, Duboué et al., 2017, McLaughlin et al., 2017). Left-right asymmetry of the habenular region is widespread among vertebrate species (Harris et al., 1996, Concha and Wilson, 2001) and, in zebrafish, the left and right dorsal habenulae (LdHb and RdHb) exhibit prominent differences in their molecular properties, connectivity and functions (deCarvalho et al., 2014, Gamse et al., 2005, Facchin et al., 2015, Duboué et al., 2017, Chou et al., 2016, Agetsuma et al., 2010, Dreosti et al., 2014). The LdHb projects to the dorsal IPN (dIPN) and ventral IPN (vIPN),

whereas RdHb neurons largely innervate the vIPN (Gamse et al., 2005). Using tract tracing in adult zebrafish, Agetsuma *et al.* (2010) found that vIPN neurons project to the dorsal raphe, and dIPN neurons to the hindbrain griseum centrale. Moreover, injection of the cell-filling dye neurobiotin into the dorsal IPN labeled cell bodies in the griseum centrale, suggesting reciprocal connectivity (Agetsuma et al., 2010). The NI and IPN are also reciprocally connected in rodents (Goto et al., 2001, Olucha-Bordonau et al., 2003). However, whether different neuronal populations in the hindbrain NI innervate distinct subregions of the IPN is unresolved.

In this study, we find that a small population of neurons defined by expression of the *goosecoid homeobox 2* (*gsc2*) gene is closely apposed to *rln3a* neurons in the zebrafish hindbrain, and distinct from neurons producing relaxin-3, cholecystokinin, and neuromedin B. Through CRISPR/Cas9-mediated targeted integration, we generated transgenic driver lines to facilitate selective labeling and manipulation of the *gsc2* and *rln3a* neuronal populations in the nucleus incertus, and found that they differ in efferent and afferent connectivity, calcium signaling, and control of locomotor behavior.

Results

Identification of *gsc2* neurons in the nucleus incertus

We initially identified the *gsc2* gene through transcriptional profiling aimed at distinguishing genes with enriched expression in the midbrain interpeduncular nucleus (IPN). IPN tissue was micro-dissected from the brains of adult zebrafish harboring *TgBAC(gng8:Eco.NfsB-2A-CAAX-GFP)*^{c375}, a transgene that labels dorsal habenular (dHb) neurons and their axons with membrane-targeted GFP in the larval and adult brain. Because GFP-labeled dHb axon terminals demarcate the IPN (deCarvalho et al., 2013), they serve as a guide to locate and excise this midbrain structure. After comparing the transcriptional profile of pooled IPN samples with remaining brain tissue, *gsc2* transcripts were identified as enriched approximately 5-fold in the IPN region relative to the rest of the brain. The *gsc2* gene encodes a protein that has homology to Goosecoid-related proteins in its homeobox domain-containing sequence. We note that the *gsc2* sequence is not annotated in the latest genome assembly (GRCz11) and was initially identified by aligning reads to Zv9 (Ensembl release 77).

From whole-mount *in situ* hybridization (WISH), we found that *gsc2* transcripts are restricted to bilateral clusters just posterior to the midbrain-hindbrain boundary and to a few sparsely distributed neurons anterior to the main cluster (Fig. 1A, A'). Double labeling with *somatostatin 1.1* (*sst1.1*), a marker of IPN neurons (Doll et al., 2011), revealed that the bilateral clusters are not situated within the IPN but rather lie dorsal to it (Fig. 1B, B').

Owing to the similar positions of *gsc2* and *rln3a* (Donizetti et al., 2008) neurons in

the larval hindbrain, we performed double-label WISH, and found that *gsc2* neurons are a distinct population, located anterior to the *rln3a* neurons (Fig. 1C, C', D).

Other neuropeptides in addition to RLN3 have been detected in the rodent NI, including neuromedin B in mice (Lu et al., 2020), and cholecystokinin (Olucha-Bordonau et al., 2003, Kubota et al., 1983) and neurotensin (Jennes et al., 1982) in rats. To determine whether transcripts encoding each of these neuropeptides are present in the zebrafish NI, we performed WISH for the zebrafish *cholecystokinin a* (*ccka*), *cholecystokinin b* (*cckb*), *neuromedin a* (*nmba*), *neuromedin b* (*nmbb*), and *neurotensin* (*nts*) genes (Fig. 1-1 A-E'). For *cholecystokinin* and *neuromedin B*, the combined expression of the two zebrafish paralogues closely resembles the overall expression pattern of each single rodent gene (Albus, 1988, Ohki-Hamazaki, 2000). Only *cckb* and *nmbb* transcripts were detected in the NI, and *nmbb* expression was also observed in the PAG (Fig. 1-1 B, D). Using double-label fluorescent WISH, we found that the *gsc2* neurons (48.33 ± 2.33 neurons) fail to express any of these neuropeptides and comprise a unique population. We found that hindbrain *nmbb* neurons (8.33 ± 1.45) are intermingled with *rln3a* neurons (10.67 ± 1.33) in the NI, with a small subset expressing both neuropeptides (Fig. 1E, Fig. 1-2 A'-C''). By contrast, *rln3a* and *nmbb* neurons exist as separate, adjacent populations in the PAG (Fig. 1-2 A). Hindbrain *cckb* neurons (4.5 ± 1.1) are a distinct population located just posterior to *rln3a* and *nmbb* neurons (Fig. 1F). From these results, we can construct a map of peptidergic neurons in the zebrafish NI (Fig. 1G), with a discrete group of *gsc2*-expressing neurons, partially overlapping expression of *rln3a* and *nmbb* in cells posterior to the *gsc2* neurons, and a distinct population of *cckb* neurons posterior to the *rln3a* and *nmbb* neurons.

gsc2 and _rln3a_ transgenic lines drive expression in the NI

To verify that the *gsc2* and *rln3a* neurons reside in the zebrafish analogue of the mammalian NI, we examined the properties of these closely apposed neuronal populations. Using CRISPR/Cas9-mediated genome integration, we generated transgenic lines to selectively label and manipulate each group. The *gsc2* and *rln3a* loci were independently targeted for integration of sequences encoding QF2 (Fig. 2A, D), a modified transcription factor that binds to the upstream activating sequence (QUAS) in the bipartite Q transcriptional regulatory system of *Neurospora crassa* (Riabinina and Potter, 2016, Subedi et al., 2014). *Tg(gsc2:QF2)*^{c721} was generated by introducing the *QF2* sequence into exon 2 of the *gsc2* gene through non-homologous end joining (Kimura et al., 2014). Another method for homology-directed integration called GeneWeld (Wierson et al., 2020) was adapted to include a secondary reporter that, together with the *QF2* sequence, was integrated into exon 1 of the *rln3a* gene to produce *Tg(rln3a:QF2, he1.1:YFP)*^{c836}. Identification of *rln3a:QF2* transgenic carriers was facilitated by inclusion of a reporter consisting of a promoter from the *hatching enzyme 1, tandem duplicate 1* (*he1.1*) gene (Xie et al., 2012) driving expression of yellow fluorescent protein (YFP) in hatching gland cells starting at 1 day post-fertilization (dpf). Because labeling is transient, the *he1.1:YFP* secondary reporter does not interfere with brain imaging of older larvae.

We confirmed that the *Tg(gsc2:QF2)*^{c721} and *Tg(rln3a:QF2, he1.1:YFP)*^{c836} driver lines recapitulate endogenous expression patterns of *gsc2* and *rln3a*, respectively, at both larval (Fig. 2B, C, E, F) and adult (Fig. 2-1 A-G) stages. Consistent with their location in the NI, the *rln3a* and *gsc2* neurons reside on the floor of the 4th ventricle (Fig.

2-1 G), with the *gsc2* neurons anterior to the *rln3a* neurons and also distributed more ventrally up to the dorsal surface of the raphe nucleus (Fig. 2-1 C). Using *TgBAC(gng8:Eco.NfsB-2A-CAAX-GFP)*^{c375} to delineate dHb axon terminals at the IPN (deCarvalho et al., 2013, Hong et al., 2013, Davison et al., 2007) we confirmed that *gsc2* neurons are located outside of the IPN in the adult brain, although a few scattered *gsc2* neurons lie just posterior and lateral to it (Fig. 2-2 A-D'). As the sparsely distributed anterior group of *gsc2* neurons are anatomically distinct from the main cluster and not within the nucleus incertus proper (Fig. 2B, C), they were excluded from subsequent analyses.

Neurotransmitter identity of *gsc2* and *rln3a* neurons

In mice (Szőnyi et al., 2019) and rats (Olucha-Bordonau et al., 2003), the NI contains a large population of GABAergic neurons, and *rln3a* NI neurons are largely GABAergic (Ma et al., 2007, Nasirova et al., 2020). To determine the neurotransmitter identity of the zebrafish *rln3a* and *gsc2* neurons, we mated doubly transgenic fish bearing *Tg(gsc2:QF2)*^{c721} or *Tg(rln3a:QF2, he1.1:YFP)*^{c836} and a QUAS reporter to fish with transgenes that either label glutamatergic neurons expressing the *solute carrier family 17 member 6b* (*slc17a6b*) gene (Miyasaka et al., 2009) or GABAergic neurons expressing *glutamate decarboxylase 1b* (*gad1b*) (Satou et al., 2013). We did not observe co-expression of *gsc2* (Fig. 3A) or *rln3a* (Fig. 3C) with the glutamatergic reporter in the NI. In contrast, an average of 82.43 ± 3.52% of neurons co-expressed GFP and mApple-CAAX in *Tg(gad1b:GFP)*^{nn25Tg}; *Tg(gsc2:QF2)*^{c721}; *Tg(QUAS:mApple-CAAX, he1.1:mCherry)*^{c636} larvae (Fig. 3D, D', G). Similarly, in *Tg(gad1b:GFP)*^{nns25};

Tg(rln3a:QF2, he1.1:YFP)^{c836}; *Tg(QUAS:mApple, he1.1:CFP)*^{c788} larvae, an average of 80.57 ± 5.57% of neurons co-expressed GFP and mApple (Fig. 3F, F', F'', G). These results indicate that *gsc2* and *rln3a* neurons are predominantly GABAergic, consistent with their NI identity.

To our knowledge, it has not been verified whether *rln3a* neurons in the periaqueductal grey are also GABAergic. We found that *rln3a* neurons in the PAG were not labeled by the glutamatergic reporter (Fig. 3B), whereas an average of 81.67 ± 3.81% showed labeling from the *gad1b* transgene (Fig. 3E, E', E'', G). This suggests that *rln3a* neurons possess similar neurotransmitter identity across neuroanatomical locations.

Distinct projection patterns of *gsc2* and *rln3a* neurons

To compare the projection patterns of *gsc2* and *rln3a* NI neurons, we expressed membrane-tagged fluorescent reporters in each group and acquired optical sections of their labeled processes using confocal microscopy. At 6 dpf, projections from *gsc2* neurons were prominent in the cerebellum, IPN, raphe, diencephalon, and rostral and caudal hypothalamus (Movie 4-1, Fig. 4A-E, Fig. 2-2B, B'). Sparse efferents from gsc2 neurons were also found in the medulla (Movie 4-1) and telencephalon (Fig. 4D). Projections from *rln3a* neurons were found in the medulla, IPN, diencephalon, lateral hypothalamus, and optic tectum (Movie 4-2, Fig. 4F-J), with some axons appearing to pass through the posterior commissure (Fig. 4G). Sparse fibers were also observed in the raphe and telencephalon (Fig. 4H, J).

Innervation of the IPN by *rln3a* neurons originates solely from the NI cluster, whereas the bulk of projections throughout the brain emanate from *rln3a* neurons in the PAG (Movie 4-2). This was confirmed by two-photon laser ablation of *rln3a* PAG neurons, which greatly reduced fibers in the medulla, diencephalon, hypothalamus and optic tectum, but spared innervation of the IPN (Fig. 4K-M). Reduction of *rln3a* PAG neuronal projections enabled visualization of those from the NI, which exclusively target the IPN (Movie 4-3, Fig. 4L). Accordingly, ablation of *rln3a* neurons solely in the NI eliminated innervation of the IPN without affecting the rest of the *rln3a* neuron projection pattern, including projections to the medulla, diencephalon, hypothalamus and optic tectum (Fig. 4M). Efferents from *gsc2* neurons were far more extensive than those of *rln3a* NI neurons, and were observed in regions not innervated by any *rln3a* neurons (e.g., cerebellum and caudal hypothalamus). Thus, the closely apposed *gsc2* and *rln3a* NI neurons exhibit divergent and largely non-overlapping projection patterns.

To examine *gsc2* and *rln3a* efferent innervation of the IPN more precisely, we used *TgBAC(gng8:Eco.NfsB-2A-CAAX-GFP)*^{c375} or *TgBAC*(*gng8:GAL4FF*)^{c426}*; Tg(UAS-E1B:NTR-mCherry)*^{c264} to delineate the IPN by labeled dHb axon terminals. We confirmed the location of *gsc2* and *rln3a* neuronal cell bodies dorsal to the IPN as visualized by nuclear-tagged reporters (Fig. 5A, A’, C’, C’). Using membrane-tagged reporters, we identified projections from both populations to the IPN (Fig. 5B, D, E-H) and found that they innervate disparate regions. This is more readily observed in sections of the adult brain in which axons of *gsc2* neurons terminate at the ventral IPN mainly along the midline neuropil (Fig. 5B, E-F’, I, K) and axons of *rln3a* neurons terminate at the dorsal IPN (Fig. 5D, G-H’, J, K), as depicted schematically in Fig. 5K.

Afferent input to the NI from the dHb-IPN pathway

Tracing studies in mice (Lu et al., 2020), rats (Goto et al., 2001, Olucha-Bordonau et al., 2003), and zebrafish (Agetsuma et al., 2010) suggest that NI neurons receive afferent input from the Hb-IPN pathway. However, it is unclear whether the Hb-IPN axis influences all NI neurons or specific populations.

To test whether the *gsc2* or *rln3a* NI neurons are regulated by the dHb-IPN network, we optogenetically activated the red-shifted opsin ReaChR (Lin et al., 2013; Wee et al., 2019) in dHb neurons using 561 nm light, while recording calcium transients in either *gsc2* or *rln3a* NI neurons under 488 nm light (Fig. 6A). We used *Tg(UAS:ReaChR-RFP)*^{jf50} to express ReaChR under control of *TgBAC*(*gng8:GAL4FF*)^{c426}, which labels dHb neurons that project to the IPN (Hong et al., 2013). To verify successful activation of dHb neurons by ReaChR, we also included *Tg(UAS:GcaMP7a)*^{zf415} to express the calcium indicator GCaMP7a (Muto et al., 2013) in dHb neurons (Fig. 6B, C). Simultaneously, we used *Tg(QUAS:GcaMP7a)*^{c594} to express GcaMP7a in either *gsc2* or *rln3a* neurons under control of *Tg(gsc2:QF2)*^{c721} or *Tg(rln3a:QF2, he1.1:YFP)*^{c836} (Fig. 6B', C').

We first confirmed that 561 nm light increases calcium signaling in ReaChR-expressing dHb neurons, but not in ReaChR-negative controls (Fig. 6D-D'', F-F'', Fig. 6-1A, D, G, J). Next, we showed that ReaChR activation in the dHb increased calcium transients in *gsc2* NI neurons, as they showed greater activation in response to 561 nm light in ReaChR-expressing larvae than in ReaChR-negative controls (Fig. 6E-E'', Fig. 6-1B, C, E, F). However, similar levels of calcium signaling were detected in the *rln3a* NI neurons of ReaChR-expressing larvae and negative controls in response to 561 nm

light (Fig. 6G-G'', Fig. 6-1H, I, K, L). Statistically significant differences in the activation of *rln3a* PAG neurons between ReaChR-expressing larvae and ReaChR-negative controls were also not detected (Fig. 6H-H'', Fig. 6-1M, N, O, P). These results show that activation of the dHb-IPN axis increases activity in *gsc2* neurons but not in *rln3a* neurons, indicating that the latter do not directly mediate functions of the dHb-IPN pathway.

Spontaneous and evoked activity differs between *gsc2* and *rln3a* neurons

In rodents, aversive stimuli, such as foot shock, air puff, water-restraint stress, exposure to an elevated plus maze, and the anxiogenic drug FG-7142 all increase neuronal activity in the NI, yet whether NI neuronal subtypes show distinct responses to aversive stimuli is unclear (Lu et al., 2020, Lawther et al., 2015, Passerin et al., 2000, Rajkumar et al., 2016, Szőnyi et al., 2019, Tanaka et al., 2005). To determine whether *gsc2* and *rln3a* neurons differ in their response to an aversive stimulus (Duboué et al., 2017), we recorded calcium transients upon delivery of a mild electric shock (25 V, 200 ms duration) to immobilized larvae (Fig. 7A, B, C). The *gsc2* neurons showed little spontaneous activity and a robust increase in calcium signaling in response to shock (Fig. 7D, D', Movie 7-1). By contrast, *rln3a* neurons showed more spontaneous fluctuations in activity throughout the recording period (Fig. 7E-H, Movie 7-2), producing a wider distribution of amplitudes (Fig. 7F-G'), and their response to shock was shorter in duration than for *gsc2* neurons (Fig. 7I). The *gsc2* and *rln3a* neurons therefore differ in their spontaneous activity and in the duration of their response to an aversive stimulus.

Ablation of *rln3a* but not *gsc2* neurons alters locomotor activity

Previous reports have implicated the NI in regulating locomotor activity and proposed that an animal's increased movement after an aversive stimulus is, in part, mediated by increased activity in the NI (Lu et al., 2020, Farooq et al., 2016). We tested whether eliminating small populations of NI neurons (i.e., 10.67 ± 1.33 *rln3a* neurons or 48.33 ± 2.33 *gsc2* neurons) would be sufficient to influence baseline locomotor behavior or the response to electric shock, which normally elicits immediate hyperactivity in larval zebrafish (Duboué et al., 2017).

With GFP expression as a guide, we used a two-photon laser to selectively ablate *gsc2* (Fig. 8A, A'), *rln3a* neurons in the NI (Fig. 8B, B'), or *rln3a* neurons in the PAG (Fig. 8C-C'''), at 6 dpf. We confirmed ablation by WISH (Fig. 8-1A, A', D, D'), and also verified selectivity by determining that *rln3a* NI neurons were spared in larvae with ablated *gsc2* neurons (Fig. 8-1B, B'), and, conversely, that *gsc2* neurons were intact in larvae with ablated *rln3a* NI neurons (Fig. 8-1C, C'). One day later (7 dpf), we tracked locomotion of individual freely swimming ablated larvae and unablated siblings for two minutes. After recording baseline activity, we delivered a single electric shock (25 V, 200 ms duration) to each larva and measured the locomotor response (Duboué et al., 2017).

Both ablated and unablated larvae exhibited hyperactivity immediately following shock (Fig. 8D-E), and statistically significant differences in the response to shock were not detected (Fig. 8E). This suggests that neither the *gsc2* neurons nor the neighboring *rln3a* neurons are required for the immediate behavioral response to shock. Unexpectedly, however, larvae that lacked *rln3a* NI neurons swam a greater overall

distance during the pre-shock period and exhibited longer phases of activity than unablated controls, larvae with ablated *gsc2* neurons, or larvae with ablated *rln3a* PAG neurons (Fig. 8F-H, Movie 8-1). Phases of activity were defined by continuous movement of the larvae with no more than one second of prolonged immobility. The total number of phases was similar in all groups (Fig. 8I). This indicates that ablation of *rln3a* NI neurons promotes prolonged phases of movement, rather than increasing the frequency of movement initiation. In addition to increased swimming, larvae that lacked *rln3a* NI neurons showed increased turning behavior. For larvae with ablated *rln3a* NI neurons, the change in angle of orientation measured per unit of distance traveled was greater than that of unablated controls, larvae with ablated *gsc2* neurons, or larvae with ablated *rln3a* PAG neurons (Fig. 8-2A). The unablated control larvae included both *Tg(gsc2:QF2)*^{c721}; *Tg(QUAS:GFP)*^{c578} and *Tg(rln3a:QF2, he1.1:YFP)*^{c836}; *Tg(QUAS:GFP)*^{c578} siblings of ablated larvae, although repeating the analyses with the control group containing only one genotype or the other did not change the conclusions (Fig. 8-2B, C, Fig. 8-3). Overall, the results show that spontaneous locomotor activity and turning behavior are increased following ablation of the *rln3a* cluster of NI neurons, whereas swimming behavior is normal after ablation of the larger *gsc2* population.

Discussion

The nucleus incertus (‘uncertain nucleus’), first described in the human brain in 1903 (Streeter, 1903), remains an enigmatic structure that has been implicated in stress (Potter et al., 1994, Bittencourt and Sawchenko, 2000, Lawther et al., 2015, Passerin et al., 2000, Rajkumar et al., 2016, Tanaka et al., 2005), arousal (Lu et al., 2020), and memory (Szőnyi et al., 2019, Ma et al., 2009). As the NI is the primary source of relaxin-3 expressing neurons in the rodent brain, they have been a focus of interest even though not all NI neurons produce this neuropeptide (Ma et al., 2013, Nasirova et al., 2020). Here, we compare the properties of the cells expressing *rln3a* with a neighboring group of neurons in the zebrafish NI.

Through transcriptional profiling, *gsc2* transcripts were found to be enriched in samples dissected from the adult zebrafish brain that encompassed the IPN. However, closer examination of both larval and adult brains revealed that *gsc2*-expressing neurons are located outside of the IPN, just anterior to the *rln3a* neurons in the NI. The enriched transcripts were likely due to the presence of *gsc2*-positive neurons that lie just posterior and lateral to the IPN. Neurons expressing the *Gsc2* murine homolog had previously been identified in the mouse brain, although there is conflicting information about their precise anatomical location (Funato et al., 2010, Gong et al., 2003, Saint-Jore et al., 1998, Gottlieb et al., 1998). On the basis of our results, we suspect that *Gsc2* neurons are not located within the rodent IPN as was previously concluded (Funato et al., 2010, Gong et al., 2003), but are likely situated adjacent to it.

We developed transgenic tools to characterize *gsc2* and *rln3a* neurons in more detail. The Gal4-UAS system of yeast is widely used in zebrafish to express reporter genes in specific cell populations; however, its utility for small groups of neurons is limited because of mosaicism due to progressive methylation of CpG residues in multicopy upstream activation sequences, resulting in transcriptional silencing (Goll et al., 2009). The QF2/QUAS system of Neurospora (Riabinina and Potter, 2016, Subedi et al., 2014), coupled with CRISPR/Cas9 integration, enabled the generation of targeted driver lines and robust and selective expression of reporter genes in either *gsc2* or *rln3a* neurons. By labeling with QUAS-driven fluorescent reporters, we determined that the anatomical location, neurotransmitter phenotype, and hodological properties of *gsc2* and *rln3a* neurons are consistent with NI identity, supporting the assertion that the griseum centrale of fish is analogous to the mammalian NI. Both groups of neurons are GABAergic, reside on the floor of the fourth ventricle and project to the interpeduncular nucleus. However, these adjacent neuronal populations have distinct connections with the IPN and other brain regions, and also differ in their afferent input, calcium signaling, and influence on locomotor behavior (summarized in Table 1). Owing that the NI has been proposed to act in concert with the median raphe and IPN, in “a midline behavior control network of the brainstem” (Goto et al., 2001), it is important to build the framework of neuronal subtypes that mediate such coordinated activity.

Table 1. Properties of *gsc2* and *rln3a* NI neurons.

	Neurotransmitter identity	Projection pattern	Projections to IPN	Spontaneous activity	Influenced by dHb-IPN pathway	Locomotion post-ablation
gsc2 neurons	0% *slc17a6b*$^+$ 82.43 ± 3.52% *gad1b*$^+$	Widespread	Ventral IPN	Low spontaneous activity	Yes	No change
rln3a NI neurons	0% *slc17a6b*$^+$ 80.57 ± 5.57% *gad1b*$^+$	Restricted to IPN	Dorsal IPN	Rhythmic calcium bursts	No	Increased

The IPN as an integrating center for dHb and NI input

Previous work demonstrated that axons from left dHb and right dHb neurons innervate different regions along the dorsoventral extent of the IPN; neurons in the left dHb project to both the dorsal IPN (dIPN) and ventral IPN (vIPN) whereas right dHb neurons mainly target the vIPN (Gamse et al., 2005). We found that different populations of NI neurons also target specific IPN compartments; *rln3a* neurons project mainly to the dIPN and *gsc2* neurons predominantly innervate the vIPN along its midline neuropil. A study by Zaupa *et al.* (2021) demonstrates that axon terminals from cholinergic and noncholinergic dHb neurons, which innervate the vIPN and dIPN respectively, show distinct patterns of activity. Spontaneous calcium spikes in cholinergic dHb terminals at the vIPN coincide with transient decreases in calcium signaling in non-cholinergic dHb terminals at the dIPN. This negatively correlated activity is mediated by activation of vIPN neurons that release GABA to inhibit non-cholinergic dHb terminals at the dIPN through their presynaptic $GABA_B$ receptors. Our results raise the possibility that innervation by different populations of NI neurons also shapes activity in the dorsal and ventral IPN. The IPN could thus integrate signals from disparate neuronal populations in the dHb and NI, and perhaps other brain regions. Future work will explore how the

activity of *rln3a* and *gsc2* axon terminals is coordinated with cholinergic and non-cholinergic dHb input to the dorsal and ventral IPN.

Distinct patterns of calcium signaling by NI neurons

Distinct patterns of activity were observed in the neuronal populations of the NI, with *gsc2* neurons having little spontaneous activity and *rln3a* neurons exhibiting continuous fluctuations in calcium signaling. A study in rats found that relaxin-3 neurons fire in synchrony with the ascending phase of the hippocampal theta oscillation (4-12 Hz), which has been implicated in spatial memory (Ma et al., 2013). Stimulation of NI neurons in rats and *Nmb* NI neurons in mice also increases hippocampal theta power (Lu et al., 2020, Nuñez et al., 2006). The oscillating calcium transients that we detected in *rln3a* neurons of larval zebrafish are on the order of seconds, however, consistent with infra-slow waves that occur at frequencies in the range of tens to hundreds of seconds, and within which fast oscillations are often nested (Palva and Palva, 2012). Infra-slow oscillations correlate with rhythmic fluctuations in performance observed in psychophysical experiments with humans, in which a subject performs a task of constant difficulty for several minutes. It has been proposed, therefore, that intra-slow waves coordinate shifts between attentive and inattentive brain states (Palva and Palva, 2012). Given that ablation of *rln3a* NI neurons increases the length of phases of movement in zebrafish larvae, fluctuating activity in *rln3a* neurons may control transitions between phases of behavioral activity and inactivity.

Cell type-specific roles for the NI

Rodent studies have described the behavior of animals with null mutations in the gene encoding RLN3 (Smith et al., 2012), or its receptor, RXFP3 (Hosken et al., 2015), and found decreased voluntary wheel running, suggesting that the relaxin-3 system is involved in regulating locomotor activity. However, it is difficult to attribute mutant phenotypes to specific sub-groups of *Rln3* neurons. Activation of the NI through microstimulation or chemogenetics increased movement in rats (Farooq et al., 2016, Ma et al., 2017), which implicates the NI region in regulating locomotor activity but does not identify the relevant neurons.

Strikingly, removal of *rln3a* NI neurons elicited hyperactivity in zebrafish larvae. Ablation of *rln3a* neurons in the PAG did not affect locomotion. This suggests that the role of the NI in regulating baseline locomotor activity is mediated by *rln3a* neurons. Because some *nmbb* neurons are interspersed with *rln3a* neurons in the NI, we cannot eliminate the possibility that loss of *nmbb* neurons also contributes to the hyperactivity phenotype. Previous studies in adult rodents indicate that enhanced NI activity promotes locomotion, but we find the opposite in larval zebrafish; NI neurons normally suppress spontaneous locomotor activity. Interestingly, a study of dopaminergic signaling in larval zebrafish also reported that dopamine suppressed spontaneous fictive swim episodes (Thirumalai and Cline, 2008), although dopamine is classically known for stimulating locomotor activity in adult rodents (Ryczko and Dubuc, 2017). Thus, differential roles for neuromodulators during development and adulthood could be a general feature of locomotor circuitry.

A number of studies have found that aversive stimuli promote expression of c-Fos in the NI (Tanaka et al., 2005, Lawther et al., 2015, Passerin et al., 2000, Rajkumar et al., 2016), leading researchers to evaluate the role of relaxin-3 in anxiety-like behaviors. In rats, intracerebroventricular infusion of a relaxin-3 receptor agonist increased entries to the open arms of an elevated plus maze and the amount of time animals spend in the light portion of a light-dark box (Ryan et al., 2013). Similar assays in mice showed that the relaxin-3 receptor agonist did not alter the basal behavioral state but rather reduced anxiety-like behavior induced by the anxiogenic drug FG-7142 (Zhang et al., 2015). However, a role for the NI in regulating the behavioral response to acute aversive stimuli has so far not been described. Lu et al., 2020 note that *Nmb* neurons in the mouse NI promote spontaneous locomotor activity and are activated in response to foot shock, a stimulus that elicits immediate locomotion, but whether they mediate the immediate locomotor response to this stimulus is unclear. Through selective ablation, we found that loss of either NI *rln3a* or *gsc2* neurons was not sufficient to alter hyperactivity normally observed in zebrafish larvae post-shock.

Previous work showed that zebrafish hindbrain *rln3a* neurons localize to a region expressing *corticotropin releasing hormone receptor 1* (*crhr1*), which encodes a receptor expressed at high levels in the rodent NI (Potter et al., 1994, Bittencourt and Sawchenko, 2000). We find that transcripts encoding neuromedin B and cholecystokinin, which have also been detected in the rodent NI (Olucha-Bordonau et al., 2003, Lu et al., 2020, Kubota et al., 1983), likewise map to the presumptive zebrafish NI. Similar to *rln3a* and *nmbb* neurons in the zebrafish larval NI, in mice *Rln3*

and *Nmb* are expressed in interspersed neuronal populations and are co-expressed in a subset of cells (Lu et al., 2020, Nasirova et al., 2020). Furthermore, we found that *cckb* neurons are a separate population located posterior to the *rln3a* and *nmbb* neurons. Szlaga *et al.* also found little overlap between cholecystokinin and relaxin-3 neurons in the rat brain (Szlaga et al., 2022). Together, these results suggest conservation of NI cell types and their organization from fish to mammals, establishing zebrafish as a model to understand the connectivity and function of the diverse types of NI neurons. Intriguingly, a new study identified a region in the zebrafish larval hindbrain, referred to as the dorsal tegmental nucleus, whose GABAergic neurons project to the dorsal IPN and are activated in conjunction with directional turning by the larva (Petrucco et al., 2023). Although the specific neuronal cell types have yet to be identified, it is likely they correspond to a subpopulation in the NI.

Materials and methods

Animals

Zebrafish were maintained at 27 °C under a 14:10 h light/dark cycle in a recirculating system with dechlorinated, filtered and heated water (system water). All lines used are listed in Table 2. Larvae were screened for labeling by fluorescent proteins using an Olympus MVX10 Macro Zoom fluorescence microscope. For imaging, larvae were incubated in system water containing 0.003% phenylthiourea (P7629, Sigma-Aldrich) to inhibit melanin pigmentation. Most analyses were performed at the larval stage, before sex determination. Analyses performed at the adult stage included both males and females. All procedures were performed in accordance with the the Institutional Animal Care and Use Committee (IACUC) of the Carnegie Institution for Science or Dartmouth College.

Table 2. Zebrafish lines used in this study.

Strain	Source	Identifier
AB	(Walker, 1998)	RRID: ZIRC_ZL1
TgBAC(gng8:Eco.NfsB-2A-CAAX-GFP)^{c375}	(deCarvalho et al., 2013)	RRID: ZFIN_ZDB-GENO-130815-4
Tg(gsc2:QF2)^{c721}	This study	N/A
Tg(rln3a:QF2, he1.1:YFP)^{c836}	This study	N/A
Tg(QUAS:GFP)^{c578}	This study	N/A
Tg(slc17a6b:DsRed)^{nns9Tg}	(Miyasaka et al., 2009)	RRID: ZFIN_ZDB-GENO-100505-14

Tg(QUAS:mApple, he1.1:CFP)^{c788}	This study	N/A
Tg(slc17a6b:EGFP)^{zf139Tg}	(Miyasaka et al., 2009)	RRID: ZFIN_ZDB-GENO-090716-2
Tg(QUAS:mApple-CAAX, he1.1:mCherry)^{c636}	This study	N/A
Tg(gad1b:GFP)^{nn25Tg}	(Satou et al., 2013)	RRID: ZFIN_ZDB-GENO-131127-6
Tg(QUAS:GFP-CAAX)^{c591}	This study	N/A
TgBAC(*gng8:GAL4FF*)^{c426}	(Hong et al., 2013)	RRID: ZFIN_ZDB-GENO-140423-3
Tg(UAS-E1B:NTR-mCherry)^{c264}	(Davison et al., 2007)	RRID: ZFIN_ZDB-GENO-070316-1
Tg(QUAS:NLS-mApple, *he1.1:CFP)*^{c718}	This study	N/A
Tg(QUAS:NLS-GFP, he1.1:CFP)^{c682}	This study	N/A
Tg(QUAS:GFP-CAAX, he1.1:YFP)^{c631}	This study	N/A
Tg(QUAS:GCaMP7a)^{c594}	This study	N/A
Tg(UAS:GCaMP7a)^{zf415}	(Muto et al., 2013)	RRID:ZFIN_ZDB-GENO-131120-53
Tg(UAS:ReaChR-RFP)^{jf50}	(Wee et al., 2019)	ZDB-ALT-201105-3

Generation of transgenic lines by Tol2 transposition

To generate *Tg(QUAS:GFP)*^{c578}, *Tg(QUAS:mApple, he1.1:CFP)*^{c788}, *Tg(QUAS:GFP-CAAX)*^{c591}, *Tg(QUAS:NLS-mApple, he1.1:CFP)*^{c718}, *Tg(QUAS:NLS-GFP; he1.1:CFP)*^{c682}, *Tg(QUAS:GFP-CAAX, he1.1:YFP)*^{c631} and *Tg(QUAS:GCaMP7a)*^{c594} transgenic lines, constructs for Tol2 transposition were produced using the MultiSite Gateway-based construction kit (Kwan et al., 2007). All plasmids used in this study and

their Addgene identifiers are listed in Table 3. For each construct, three entry vectors were first assembled by BP reactions (11789020, Thermo Fisher Scientific). A 16 bp *QUAS* sequence (Potter et al., 2010) was cloned into the 5' entry vector (*pDONRP4-P1R*, #219 of Tol2kit v1.2). DNA encoding GFP (green fluorescent protein) or mApple, or those sequences with an added nuclear localization sequence (NLS) or membrane localization sequence (CAAX) was inserted into middle entry vectors (*pDONR221*, #218 of Tol2kit v1.2). Sequences corresponding to the *SV40 poly A* tail, or the *poly A* tail followed by a secondary marker consisting of the zebrafish *hatching enzyme 1, tandem duplicate 1* (*he1.1*) promoter (Xie et al., 2012) driving CFP (cyan fluorescent protein) or YFP (yellow fluorescent protein), were placed into the 3' entry vector (*pDONRP2R-P3*, #220 of Tol2kit v1.2). All three entry vectors were introduced into a Tol2 destination construct (*pDestTol2pA2*, #394 of the Tol2kit v1.2) using an LR reaction (11791020, Thermo Fisher Scientific).

To produce mRNA encoding Tol2 transposase, *pCS-zT2TP* (Suster et al., 2009) was digested with *Not*I and RNA was synthesized *in vitro* using the mMESSAGE mMACHINE Transcription Kit with SP6 polymerase (AM1340, Thermo Fisher Scientific). RNA was extracted with phenol/chloroform-isoamyl alcohol, re-extracted with chloroform, and precipitated with isopropanol. A solution containing *QUAS* plasmid DNA (25 ng/µl), Tol2 transposase mRNA (25 ng/µl) and phenol red (0.5%) was microinjected into one-cell stage zebrafish embryos that were raised to adulthood. Transgenic founders were identified by screening their F_1 progeny for fluorescently labeled hatching gland cells at 1 dpf and for labeling in the brain under QUAS control.

Generation of transgenic lines by genome editing

Methods for CRISPR/Cas9-targeted integration were used to generate the *Tg(gsc2:QF2)*^{c721} and *Tg(rln3a:QF2, he1.1:YFP)*^{c836} driver lines. For *Tg(gsc2:QF2)*^{c721}, the non-homologous end joining technique described by Kimura et al. (2014) was modified by integration of a *QF2* donor plasmid, *Gbait-hsp70-QF2-pA* (Addgene plasmid #122563), which contains a GFP bait sequence for Cas9-mediated linearization of the donor plasmid (Kimura et al., 2014). Cas9 RNA (Jao et al., 2013) and sgRNAs (Hwang et al., 2013) targeting *gsc2* or the GFP bait sequence (Auer et al., 2014) were synthesized as previously described. Briefly, pairs of synthetic oligonucleotides (*gsc2*_sense, *gsc2*_anti-sense Table 4), containing the overhangs 5'-TAGG-N_{18}-3' (sense) or 5'-AAAC-N_{18}-3' (anti-sense), were annealed to each other. The resulting DNA was cloned into the *pDR274* vector (Addgene, plasmid #42250; Hwang et al., 2013) following digestion of *pDR274* with *Bsa*I (R3733S, New England Biolabs). The *pDR274* templates and the *pDR274* vector for synthesis of the GFP bait sgRNA (Auer et al., 2014) were digested by *Dra*I and sgRNAs synthesized using the MAXIscript T7 Transcription Kit (AM1312, Thermo Fisher Scientific). *pT3TS-nCas9n* template DNA (Addgene, plasmid #46757; Jao et al., 2013) was digested with *Xba*I (R0145S, New England Biolabs), and Cas9 RNA was synthesized using the mMESSAGE mMACHINE Transcription Kit (AM1348, Fisher Scientific). For each transgenic line, a solution containing the sgRNA targeting the gene of interest (50 ng/µl), GFP bait sgRNA (50 ng/µl), the *Gbait-hsp70-QF2-pA* plasmid (50 ng/µl), Cas9 mRNA (500 ng/µl), and phenol red (0.5%) was microinjected into one-cell stage embryos.

For *Tg(rln3a:QF2, he1.1:YFP)*^{c836}, the GeneWeld approach described by Wierson *et al*., which uses short homology arms to facilitate integration by homology-directed repair, was modified by introduction of *QF2* and *he1.1:YFP* sequences into the donor vector (Wierson et al., 2020). The resulting *pPRISM-QF2-he1.1:YFP* donor construct contains two target sites for a universal sgRNA (ugRNA) that flank the cargo: a 2A self-cleaving sequence, *QF2*, and the *he1.1:YFP* secondary marker. To generate the construct, four PCR products were produced. *QF2* was amplified from *Gbait-hsp70-QF2-pA* (Addgene plasmid #122563; Choi et al., 2021; 2A_*QF2*_F, 2A_*QF2*_R, Table 4). The *he1.1:YFP* cassette (*he1.1:YFP*_F, *he1.1:YFP*_R, Table 4) was amplified from *p3E_he1a:YFP* (Addgene, plasmid #113879), and the polyA terminator (polyA_F, polyA_R, Table 3) and plasmid backbone (Col1E_F, Col1E_R, Table 4) were amplified from *pPRISM-Stop-cmlc2-eGFP* (Addgene kit #1000000154; Wierson et al., 2020). The PCR-amplified fragments were assembled using NEBuilder HiFi DNA Assembly Cloning Kit (E5520S, New England Biosystems).

To produce *rln3a* homology arms, complementary oligonucleotide pairs (*rln3a*_5'arm_sense, *rln3a*_5'arm_anti-sense; *rln3a*_3'arm_sense, *rln3a*_3'arm_anti-sense, Table 4) were designed using GTagHD (Wierson et al., 2020) and annealed to each other. The *pPRISM-QF2-he1.1:YFP* donor vector was first digested with *BfuA*I and *BspQ*I, (R0701S and R0712S, New England Biolabs) and then combined with the homology arms in a ligation reaction (M0202S, New England Biolabs). To synthesize ugRNA and an sgRNA targeting the *rln3a* gene, synthetic oligonucleotide pairs (*rln3a*_sense, ugRNA_sense, common_anti-sense, Table 4) were annealed to each other, elongated by Phusion polymerase (M0530S, New England Biolabs), and used as

templates for *in vitro* transcription with the MAXIscript T7 Transcription Kit (AM1312, Thermo Fisher Scientific). A solution containing *rln3a* sgRNA (50 ng/µl), universal sgRNA (50 ng/µl), the *pPRISM-QF2-he1.1:YFP-rln3a-HA* donor plasmid (100 ng/µl), Cas9 mRNA (500 ng/µl), and phenol red (0.5%) was microinjected into one-cell stage embryos.

When applicable, injected embryos were screened for labeling by fluorescent proteins in the hatching gland. To verify successful integration, PCR was performed on genomic DNA from injected embryos using primers that flank the integration site, with the forward primer corresponding to genomic sequence and the reverse primer corresponding to donor plasmid sequence (*gsc2*_val_F, hsp70_R; *rln3a*_val_F, *QF2*_R, Table 4). Sanger sequencing confirmed the identity of PCR products. Transgenic founders were identified by breeding F_0 adults with a *QUAS* reporter line and screening progeny for fluorescent labeling of the hatching gland when applicable, and for labeling by QUAS-driven fluorescent reporters. PCR and sequencing were repeated in F_1 larvae to confirm integration at the correct target site.

Table 3. Plasmids used in this study.

Plasmid	**Source**	**Identifier**
pDestTol2-QUAS:GFP	This manuscript	Addgene plasmid #184811
pDestTol2-QUAS:mApple-he1.1:CFP	This manuscript	Addgene plasmid #184812
pDestTol2-QUAS:GFP-CAAX	This manuscript	Addgene plasmid #184813

pDestTol2-QUAS:NLS-mApple-he1.1:CFP	This manuscript	Addgene plasmid #184814
pDestTol2-QUAS:NLS-GFP-he1.1:CFP	This manuscript	Addgene plasmid #184815
pDestTol2-QUAS:GFP-CAAX-he1.1:YFP	This manuscript	Addgene plasmid #184816
pDestTol2-QUAS:GCaMP7a	This manuscript	Addgene plasmid #184817
pCS-zT2TP	(Suster et al., 2009)	N/A
Gbait-hsp70-QF2-pA	(Choi et al., 2021)	Addgene plasmid #122563
pDR274	(Hwang et al., 2013)	Addgene plasmid #42250
pDR274-gsc2-sgRNA	This manuscript	Addgene plasmid #184818
pDR274-GFPbait-sgRNA	(Auer et al., 2014)	N/A
pT3TS-nCas9n	(Jao et al., 2013)	Addgene plasmid #46757
pPRISM-QF2-he1.1:YFP	This manuscript	Addgene plasmid #184819
p3E_he1a:YFP	Addgene	Addgene plasmid #113879
pPRISM-Stop-cmlc2-eGFP	(Wierson et al., 2020)	Addgene kit #1000000154
pPRISM-QF2-he1.1:YFP-rln3a-HA	This manuscript	Addgene plasmid #184820

TOPO-nmba	This manuscript	Addgene plasmid #184821
TOPO-nmbb	This manuscript	Addgene plasmid #184822
TOPO-nts	This manuscript	Addgene plasmid #184823
pSPORT-sst1.1	(Argenton et al., 1999)	N/A

Table 4. Oligonucleotides used in this study.

Oligonucleotide	**Sequence**
*gsc2*_sense	5'TAGGTCACCGCACCATCTTCACAG3'
*gsc2*_anti-sense	5'AACCTGTGAAGATGGTGCGGTGA3'
2A_*QF2*_F	5'AAACCCCGGTCCTATGCCACCCAAGCGCAAA3'
2A_*QF2*_R	5'TTAATTACTAGTTTCACTGTTCGTATGTATTAATGTCGGAG3'
*he1.1:YFP*_F	5'TAGTTCTTTAAACTCAACCACTCCAGGCATAGC3'
*he1.1:YFP*_R	5'TCCGCCTCAGAAGCCATAGAGCCCACCGCATC3'
polyA_F	5'TACGAACAGTGAAACTAGTAATTAAGTCTCAGCCAC3'
polyA_R	5'TGGAGTGGTTGAGTTTAAAGAACTAGGAACGCC3'
Col1E_F	5'TGGGCTCTATGGCTTCTGAGGCGGAAAGAAC3'
Col1E_R	5'CTTGGGTGGCATAGGACCGGGGTTTTCTTC3'
rln3a_5'arm_sense	5'GCGGTTTCTCGGCTCTCGTAGTGTGTCTGCTGCTGGCTGGAGTAAA GGCGCTGGAC3'
rln3a_5'arm_anti-sense	5'GAAGGTCCAGCGCCTTTACTCCAGCCAGCAGCAGACACACTACGA GAGCCGAGAAA3'
rln3a_3'arm_sense	5'CGGTTTCGGATGAACTCCCTGCCGCATAATTTGACTCCATACGAGG GCCCGGCG3'

*rln3a*_3'arm_anti-sense	5'AAGCGCCGGGCCCTCGTATGGAGTCAAATTATGCGGCAGGGAGTTCATCCGAAA3'
*rln3a*_sense	5'TAATACGACTCACTATAGGAGTAAAGGCGCTGGACGCGTTTTAGAGCTAGAAATAGC3'
ugRNA_sense	5'TAATACGACTCACTATAGGGAGGCGTTCGGGCCACAGGTTTTAGAGCTAGAAATAGC3'
common_anti-sense	5'AAAAGCACCGACTCGGTGCCACTTTTTCAAGTTGATAACGGACTAGCCTTATTTTAACTTGCTATTTCTAGCTCTAAAAC3'
*gsc2*_val_F	5'GTCTGGGGAAAGCGTGTGTT3'
*hsp70*_R	5'TCAAGTCGCTTCTCTTCGGT3'
*rln3a*_val_F	5'CGCTTTTGTTTCCAGAAAGG3'
*QF2*_R	5'CAGACCCGGAGTATCGATGT3'
*gsc2*_F	5'GTGCAGGACAAGAGGAGCTT3'
*gsc2*_R	5'GTTTCAATTTAGGTGACACTATAGTCCTCGAAGACTGAAGGGAA3'
*rln3a*_F	5'CACAGATGAAATCCTGGACTTGT3'
*rln3a*_R	5'GTTTCAATTTAGGTGACACTATAGCTGAAATGAGAGAGCGAGCA3'
*ccka*_F	5'TCTGTGTATGTGCCCTGCTG3'
*ccka*_R	5'GTTTCAATTTAGGTGACACTATAGTGGCCAGTAGTTCGGTTAGG3'
*cckb*_F	5'GGGGTGTGTGTGTGTGTGAT3'
*cckb*_R	5'GTTTCAATTTAGGTGACACTAGAGATGAGTTTGGCCAGCAG3'
*nmba*_F	5'ATGGCTGATGATGGACATTG3'
*nmba*_R	5'CATCCTGTTGGCCAATTCTT3'
*nmbb*_F	5'CAGTCCAAGCGTATCCAGGT3'
*nmbb*_R	5'TCATTTATTGTCTTGAATGTAGCTTT3'
*nts*_F	5'TTGTGTGTTTTCTCCCTCTTCA3'
*nts*_R	5'CGGCCGTCTGGATTTATTAG3'

611

RNA *in situ* hybridization

DNA templates for *gsc2*, *rln3a*, *ccka*, *cckb* probes were generated using PCR to incorporate a binding site for SP6 polymerase. cDNA for PCR amplification was obtained by reverse transcription of RNA extracted from 6 dpf embryos with TRIzol (15596026, Invitrogen) using the QuantiTect Reverse Transcription kit (205311, Qiagen). DNA templates were amplified with the following PCR primers: *gsc2*_F, *gsc2*_R, *rln3a*_F, *rln3a*_R, *ccka*_F, *ccka*_R, *cckb*_F, and *cckb*_R (Table 4). DNA templates for *nmba*, *nmbb* and *nts* were amplified from cDNA (*nmba*_F, *nmba*_R, *nmbb*_F, *nmbb*_R, *nts*_F, *nts*_R, Table 4), cloned using the TOPO TA kit (K465001, Invitrogen), and linearized by digestion with *BamH*I (R0136S, New England Biolabs). The template for the *sst1.1* probe was a cDNA clone in a *pSPORT1* vector (Argenton et al., 1999) linearized by digestion with *Sal*I (R3138L, New England Biolabs).

DNA templates were used for digoxigenin (DIG)-labeled *in vitro* transcription of *gsc2*, *rln3a*, *ccka*, *cckb*, *nmba*, *nmbb* and *nts* probes (11175025910, Roche) and fluorescein (FITC)-labeled *in vitro* transcription of *rln3a* and *sst1.1* probes (11685619910, Roche). The *gsc2*, *rln3a*, *ccka*, *cckb*, and *sst1.1* probes were synthesized with SP6 polymerase and the *nmba*, *nmbb*, and *nts* probes with T7 polymerase (Fisher Scientific, EP0113). RNA probes were purified using illustra MicroSpin G-50 Columns (27533001, GE Healthcare).

For whole-mount RNA *in situ* hybridization (Thisse et al., 1993, Liang et al., 2000), larvae and dissected adult brains were fixed overnight in paraformaldehyde (PFA; 4% in 1x phosphate-buffered saline) at 4°C then dehydrated overnight in 100% methanol (A4124, Fisher Scientific) at -20°C. Tissue was rehydrated stepwise in

methanol/phosphate-buffered saline (PBS) and washed with PBT (1x PBS, 0.1% Tween 20). Larvae were digested for 30 minutes and dissected adult brains for 35 minutes in proteinase K (3115836001, Roche; 10 µg/ml in PBT). To stop the reaction, tissue was fixed in 4% PFA at room temperature for 20 minutes, then washed with PBT. Specimens were prehybridized for at least two hours at 70°C in hybridization buffer [50% formamide (17899, Fisher Scientific), 5X saline sodium citrate (SSC), 50 µg/ml heparin (H3393, Sigma-Aldrich), 500 µg/ml tRNA (10109525001, Sigma-Aldrich), 0.1% Tween 20 (P1379, Sigma-Aldrich), 9 mM citric acid] with 5% dextran and then hybridized overnight at 70°C in hybridization buffer with 5% dextran and 30 ng of probe. Samples were then washed in hybridization buffer (without dextran), transitioned stepwise at 70°C from hybridization buffer to 2X SSC, washed twice for 30 minutes in 0.2x SSC at 70°C, and transitioned stepwise into PBT at room temperature. Adult brains were embedded in 4% low melting point agarose (50100, Lonza) and sectioned (70 µm) using a Leica VT1000s vibratome. Whole mount larvae and adult brain sections layered on glass slides were blocked for at least one hour in PBT with 2 mg/ml bovine serum albumin and 2% sheep serum at room temperature and then incubated overnight at 4°C with alkaline phosphatase-coupled anti-DIG antiserum (11093274910, Roche) diluted 1/5000 in blocking solution. Samples were washed several times in PBT, and detection with 4-Nitro blue tetrazolium chloride (NBT; 11383213001, Roche) and 5-bromo-4-chloro-3-indolyl-phosphate (BCIP; 11383221001, Roche) was performed in alkaline phosphatase reaction buffer [100 mM Tris pH 9.5, 50 mM $MgCl_2$, 100 mM NaCl, 0.1% Tween 20].

For colorimetric double *in situ* hybridization reactions, larvae were hybridized with DIG and FITC probes simultaneously as previously described (Liang et al., 2000), and the DIG probe was first detected using NBT/BCIP as above. To inactivate alkaline phosphatase, larvae were post-fixed overnight at room temperature in 4% PFA, washed twice for 20 minutes each with MABT [100 mM maleic acid, 150 mM NaCl, 0.1% Tween-20, pH 7.5], incubated for 10 minutes at 70°C in EDTA (10 mM in MABT), and dehydrated in methanol for 10 minutes. Samples were rehydrated stepwise in methanol/MABT, washed in MABT, and blocked for 1 hour in blocking buffer consisting of 20% sheep serum and 2% blocking reagent (11096176001, Roche) in MABT. Tissues were incubated overnight at 4°C in alkaline phosphatase-coupled anti-FITC antiserum (11426338910, Roche) diluted 1:5000 in blocking buffer. Finally, samples were washed several times in MABT. FITC detection with BCIP and iodo-nitrotetrazolium violet was performed in alkaline phosphatase buffer with 10% polyvinyl alcohol. Samples were cleared in glycerol and mounted for imaging using a Zeiss Axioskop microscope fitted with a Leica DFC 500 digital color camera and Leica Applications Suite software.

For fluorescent double *in situ* hybridization, larvae were fixed in 4% PFA, dehydrated in methanol, and incubated in 2% hydrogen peroxide in methanol for 20 minutes. After rehydration and washing in PBT as above, larvae were digested for 30 minutes in 20 µg/ml proteinase K in PBT, post-fixed in 4% PFA, washed, prehybridized, and hybridized overnight at 70°C in hybridization buffer with 5% dextran and 40 ng each of DIG and FITC probes. Stringency washes were performed as above, then larvae were washed in TNT [0.1M Tris pH 7.5, 0.1M NaCl, 0.1% Tween-20] and maintained for

2 hours in 2% blocking reagent (11096176001, Roche) in TNT. Larvae were incubated overnight at 4°C in horseradish peroxidase-coupled anti-FITC antiserum (11426346910, Roche) diluted 1:500 in blocking solution, then washed several times in TNT. FITC detection was performed using TSA Plus fluorescein diluted 1:50 in amplification diluent (NEL741001KT, Akoya Biosciences). Samples were washed several times in TNT, incubated in 1% hydrogen peroxide in TNT for 20 minutes, washed again in TNT, blocked as above for 1 hour, and incubated overnight at 4°C in horseradish peroxidase-coupled anti-DIG antiserum (11207733910, Roche) diluted 1:500 in blocking solution. Tissue was washed several more times in TNT and DIG detection was performed using TSA Plus Cyanine diluted 1:50 in amplification diluent (NEL744001KT, Akoya Biosciences). Fluorescently labeled samples were imaged using confocal microscopy.

Confocal imaging

Larvae were anesthetized in 0.02% tricaine and individually mounted in a droplet of 1.5% low melting point agarose (50100, Lonza) centered in a 60 mm x 15 mm Petri dish. After the agarose solidified, system water with 0.02% tricaine was added to each dish. Larvae were imaged using either a Leica SP5 with a 25X (NA = 0.95) water immersion objective, or a Zeiss LSM 980 with a 20X (NA = 0.5) water immersion objective.

Adult brains were fixed overnight in 4% PFA at 4°C, rinsed in 1x PBS, and mounted in 4% low melting point agarose (50100, Lonza) for sectioning (70 μm) by a Leica VT1000s vibratome. Sections were mounted in glycerol for imaging under either a

Leica SP5 with a 20X (NA = 0.7) objective or a Zeiss LSM 980 with a 20X (NA = 0.8) objective.

Z-stacks of the larval brain encompassing fluorescent signals included approximately 125 slices and 250 µm for dorsal views, or 75 slices and 150 µm for lateral views. Z-stacks focused only on the NI included approximately 35 slices and 70 µm from a dorsal or lateral view. Z-stacks of adult brain sections included 35 slices and 70 um.

Calcium signaling

Larvae were paralyzed by a 1 minute immersion in α-bungarotoxin (20 µl of 1 mg/ml solution in system water; B1601, ThermoFisher Scientific), followed by washing in fresh system water (Duboué et al., 2017, Baraban, 2013, Severi et al., 2014). Individual larvae were embedded in a droplet of 1.5% low melting point agarose (50100, Lonza) centered in a 60 mm x 15 mm Petri dish. After the agarose solidified, system water was added to the dish. For all calcium signaling experiments, larvae were imaged in *xyt* acquisition mode using a Zeiss LSM 980 with a 20X (NA=0.5) water immersion objective and a 488 nm laser.

To record calcium transients in response to electric shock, a plastic ring holding electrodes that were connected to a Grass SD9 electrical stimulator (Grass Instruments), was placed in each dish. Images of *gsc2* or *rln3a* NI neurons were acquired at 475 x 475 pixel resolution and a rate of 5.2 Hz. Calcium transients were recorded for 600 frames (115.4 s) for baseline measurements, then larvae were

shocked once (25V, 200 ms duration) and 1400-1800 more frames (269.2-346.2 s) collected.

To record calcium transients in response to stimulation of the red-shifted opsin ReaChR (Lin et al., 2013) with 561 nm light, images were first acquired using a 488 nm laser at 310 x 310 pixel resolution and a rate of 2.6 Hz. The Z-depth was adjusted to the plane of the neuronal population being imaged (i.e., dHb, NI or PAG brain regions). Spontaneous calcium transients were recorded for 200 frames (76.9 s), the 561 nm laser was activated at 5% power while 20 more frames (7.7 s) were acquired, and then calcium transients were recorded for another 150 frames (57.7 s).

For all calcium imaging experiments, individual frames were extracted in Fiji (Schindelin et al., 2012) using *File -> Save As -> Image Sequence*) and imported to MATLAB, where mean fluorescence intensities for regions of interest (ROI) were calculated. Briefly, a high contrast image was generated for each larva by calculating a maximum intensity projection of its image series. ROIs were drawn manually using the high contrast image and the MATLAB function *roipoly*. For recordings of *gsc2* or *rln3a* neurons, ROIs were individual neurons; for dHb recordings, each dHb nucleus was designated as an ROI. Mean fluorescence intensity of pixels within each ROI was calculated. ΔF/F was calculated according to the following formula:

$$F \leftarrow \frac{F_i - F_{min}}{F_{max} - F_{min}}$$

where F_i indicates the mean fluorescence intensity in an ROI at each time point, and F_{max} and F_{min} are the maximum and minimum fluorescence values respectively for that ROI during the recording period. To calculate total activity before and after the stimulus, ΔF/F was averaged across ROIs for each larva and the total activity was obtained for

the time period by calculating the area under the curve using the MATLAB function *trapz*.

The initial time point at which neuronal activity increased for a given ROI was calculated using the MATLAB *findpeaks* function (MinPeakProminence: 0.2, MinPeakWidth: 10).

Two-photon laser-mediated cell ablation

At 6 dpf, *Tg(gsc2:QF2)*^{c721}; *Tg(QUAS:GFP)*^{c578} or *Tg(rln3a:QF2, he1.1:YFP)*^{c836}; *Tg(QUAS:GFP)*^{c578} larvae were anesthetized in 0.02% tricaine and individually mounted within a droplet of 1.5% low melting point agarose (50100, Lonza) centered in a 30 mm x 10 mm Petri dish. After the agarose solidified, system water was added. GFP-expressing cells were located using a two-photon microscope (Bruker) with a 60X (NA = 1) objective. The laser was tuned to 885 nm and, using GFP labeling as a guide, was focused on the relevant neuronal population and activated for several seconds at maximum power until the GFP signal disappeared. Because the two-photon laser power is delivered to a restricted Z-plane, ablations were repeated at multiple depths to eliminate each cell population. For ablation of *gsc2* neurons the laser was activated over an area of 600-2000 μm^2 on four Z-planes. The laser was activated over an area of 1000-1250 μm^2 on two Z-planes for ablation of *rln3a* NI neurons and over an area of 1200-1800 um^2 on two Z-planes for removal of each *rln3a* PAG nucleus (left and right).

Locomotor assay

Behavioral experiments were performed blind to the ablation status of each larva being assayed. Unablated controls were a mixture of *Tg(gsc2:QF2)*^{c721}; *Tg(QUAS:GFP)*^{c578} and *Tg(rln3a:QF2, he1.1:YFP)*^{c836}; *Tg(QUAS:GFP)*^{c578}, and were siblings of ablated larvae. Behavioral tests were conducted in a temperature-controlled room (27° C) on individual 7 dpf larvae. The 6 cm^3 acrylic testing chamber had a 0.5 cm platform on which a 40 mm cell strainer (Falcon) was placed. The chamber was filled with fresh system water and set on top of an infrared illumination source (880 nm, ViewPoint Life Sciences). Locomotor activity was recorded by a high frame rate charged-coupled device (CCD) camera (Point Grey Research), which was connected to a computer (Dell). Tracking was performed in real time at 60 frames per second, using ZebraLab software (ViewPoint Life Sciences). Swimming behavior was recorded for 120 seconds, then each larva was shocked once (25 V, 200 ms duration), and activity recorded for an additional 120 seconds. To analyze locomotor activity, the x and y coordinates of a larva's position in each frame were exported from ZebraLab. Activity was quantified using R statistical software (R Core Team) according to the following equation:

$$D = \sqrt{(x_{i+1} - x_i)^2 + (y_{i+1} - y_i)^2}$$

where i indicates a single frame. Total distances were calculated by summing the distance for all frames over the relevant period of the recording. Total number of movement phases and average length of movement phases during the pre-shock period were calculated for each larva using R statistical software (R Core Team). Movement trajectories were plotted using MATLAB. Phases of movement and their durations were extracted using R statistical software by first binning the distances for all

frames within each second of the recording, then iterating through each subsequent second. A movement phase was determined to commence when there was movement within a given second and no movement in the preceding second, and the phase persisted for each subsequent consecutive second with movement. The phase of movement was determined to end when there was no movement within a given second following one with movement. Turning behavior was quantified using R statistical software by iterating through the x and y coordinates of a larva's position in each frame. Starting with the second frame, the size of the angle formed by the larva's change in orientation between the first and second frame, and the second and third frame, was calculated according to the law of cosines:

$$C = \cos^{-1}((a^2 + b^2 - c^2)/2ab)$$

where C is the angle formed by two lines of length a and b, and c is the length of the side opposite angle C. Total turning was calculated by summing the size, in degrees, of all calculated angles of all frames in which a larva was active. Total turning for each larva was divided by the total distance traveled to calculate a ratio of turning per unit of distance traveled.

Quantification and statistical analyses

All means are presented with standard error of the mean. Statistical details for all experiments are summarized in Table 5. Data structure was determined using Shapiro-Wilk tests. Statistical analyses were performed using either R statistical software (R Core Team) or MATLAB. Sample sizes were similar to those typically used in zebrafish behavior and calcium imaging studies (Agetsuma et al., 2010, Duboué et al., 2017, Choi

et al., 2021, Facchin et al., 2015, Wee et al., 2019, Muto et al., 2013). Data were plotted using the MATLAB library PlotPub (K M Masum Habib, 2022) or the R package ggplot2 (Hadley Wickham, 2016). Where applicable, larvae were randomized to the treatment or control group, and no larvae were excluded.

Table 5. Summary of Statistical Tests Used

Figure	Panel	Data Structure	Type of test	p value
6	D''	Normal	Two-sample t-test	p = 0.00041
6	E''	Normal	Two-sample t-test	p = 0.0073
6	F''	Non-parametric	Wilcoxon rank sum test	p = 0.032
6	G''	Normal	Two-sample t-test	p = 0.83
6	H''	Normal	Two-sample t-test	p = 0.45
7	H	Normal	Two-sample t-test	p = 0.0035
7	I	Non-parametric	Wilcoxon rank sum test	p = 0.04
8	E	Non-parametric	Kruskal-Wallis rank-sum test with Dunn's all-pairs test	Kruskal-Wallis: $p = 2.2 \times 10^{-16}$. Dunn's post-hoc tests: no statistically significant differences within pre-shock and post-shock groups, $p < 0.001$ for each pre-shock vs. post-shock comparison.
8	G	Non-parametric	Kruskal-Wallis rank-sum test with Dunn's all-pairs test	Kruskal-Wallis: p = 0.00099. *rln3a* NI neurons ablated vs. unablated p = 0.0019 *rln3a* NI neurons ablated vs. *gsc2* neurons ablated p = 0.0019

				rln3a NI neurons ablated vs. *rln3a* PAG neurons ablated p = 0.0019.
8	H	Non-parametric	Kruskal-Wallis rank-sum test with Dunn's all-pairs test	Kruskal-Wallis: p = 0.0013. *rln3a* NI neurons ablated vs. unablated p = 0.039, *rln3a* NI neurons ablated vs. *gsc2* neurons ablated p = 0.039, *rln3a* NI neurons ablated vs. *rln3a* PAG neurons ablated p = 0.00055.
8	I	Non-parametric	Kruskal-Wallis rank-sum test with Dunn's all-pairs test	p = 0.89
8-2	A	Non-parametric	Kruskal-Wallis rank-sum test with Dunn's all-pairs test	Kruskal-Wallis: p = 0.00017. ablated *rln3a* NI neurons vs. unablated p = 0.00038, ablated *rln3a* vs. *gsc2* NI neurons p = 0.00066, or ablated *rln3a* NI vs. *rln3a* PAG neurons p = 0.00066.
8-2	B	Non-parametric	Kruskal-Wallis rank-sum test with Dunn's all-pairs test	Kruskal-Wallis: p = 0.000097. ablated *rln3a* NI neurons vs. unablated p = 0.00057, ablated *rln3a* vs. *gsc2* NI neurons p = 0.00059, or ablated *rln3a* NI vs. *rln3a* PAG neurons p = 0.00061.
8-2	C	Non-parametric	Kruskal-Wallis rank-sum test with Dunn's all-pairs test	Kruskal-Wallis: p = 0.00045. ablated *rln3a* NI neurons vs. unablated p = 0.0045, ablated *rln3a* vs. *gsc2* NI neurons p =

				0.001, or ablated *rln3a* NI vs. *rln3a* PAG neurons p = 0.001.
8-3	A	Non-parametric	Kruskal-Wallis rank-sum test with Dunn's all-pairs test	Kruskal-Wallis: $p = 4.74 \times 10^{-15}$. Dunn's post-hoc tests with adjustment for multiple comparisons: no statistically significant differences within pre-shock and post-shock groups, $p < 0.001$ for each pre-shock vs. post-shock comparison.
8-3	B	Non-parametric	Kruskal-Wallis rank-sum test with Dunn's all-pairs test	Kruskal-Wallis: p = p = 2.85×10^{-16}. Dunn's post-hoc tests with adjustment for multiple comparisons: no statistically significant differences within pre-shock and post-shock groups, $p < 0.001$ for each pre-shock vs. post-shock comparison.
8-3	C	Non-parametric	Kruskal-Wallis rank-sum test with Dunn's all-pairs test	Kruskal-Wallis: p = 0.0012. ablated *rln3a* NI neurons vs. unablated p = 0.012, ablated *rln3a* vs. *gsc2* NI neurons p = 0.0023, or ablated *rln3a* NI vs. *rln3a* PAG neurons p = 0.0023.
8-3	D	Non-parametric	Kruskal-Wallis rank-sum test with Dunn's all-pairs test	Kruskal-Wallis: p = 0.0018. ablated *rln3a* NI neurons vs. unablated p = 0.098, ablated *rln3a* vs. *gsc2* NI neurons ablated p = 0.060, or

				ablated *rln3a* NI vs. *rln3a* PAG neurons p = 0.00076.
8-3	E	Non-parametric	Kruskal-Wallis rank-sum test with Dunn's all-pairs test	p = 0.87
8-3	F	Non-parametric	Kruskal-Wallis rank-sum test with Dunn's all-pairs test	Kruskal-Wallis: p = 0.0012. ablated *rln3a* NI neurons vs. unablated p = 0.0078, ablated *rln3a* vs. *gsc2* NI neurons p = 0.0022, or ablated *rln3a* NI vs. *rln3a* PAG neurons p = 0.0022.
8-3	G	Non-parametric	Kruskal-Wallis rank-sum test with Dunn's all-pairs test	Kruskal-Wallis: p = 0.0012. ablated *rln3a* NI neurons vs. unablated p = 0.099, ablated *rln3a* vs. *gsc2* NI neurons ablated p = 0.042, or ablated *rln3a* NI vs. *rln3a* PAG neurons p = 0.00049.
8-3	H	Non-parametric	Kruskal-Wallis rank-sum test with Dunn's all-pairs test	p = 0.90

Data and Code Availability

Raw data have been deposited at Mendeley Data and are publicly available as of the date of publication. All original code has been deposited at Zenodo and is publicly available. DOIs for data and code are listed in Table 6.

Table 6. Deposited data and code.

Item	Location	DOI
Raw data—part 1	Mendeley Data	http://dx.doi.org/10.17632/tm2bjzjp5g.1
Raw data—part 2	Mendeley Data	http://dx.doi.org/10.17632/mcbdr53ppt.1
Raw data—part 3	Mendeley Data	http://dx.doi.org/10.17632/3vrhjh6xrp.1
Raw data—part 4	Mendeley Data	http://dx.doi.org/10.17632/p9nd6mf7w2.1
Raw data—part 5	Mendeley Data	http://dx.doi.org/10.17632/pmpxtfv2ps.1
Raw data—part 6	Mendeley Data	http://dx.doi.org/10.17632/xwtjpvd885.1
Figure 6 code	Zenodo	http://dx.doi.org/10.5281/zenodo.6412939
Figure 7 code	Zenodo	http://dx.doi.org/10.5281/zenodo.6412965
Figure 8 code	Zenodo	http://dx.doi.org/10.5281/zenodo.6412969
Movie 8-1 code	Zenodo	http://dx.doi.org/10.5281/zenodo.6412978

Figure Legends

Figure 1. *gsc2* neurons localize to the nucleus incertus.

(A, A') WISH for *gsc2* and (B-C') double-label WISH for (B, B') *gsc2* and *sst1.1* or (C, C') *gsc2* and *rln3a* was performed on (A-B') 4 days post-fertilization (dpf) or (C, C') 6 dpf larvae. (A, C, C') Dorsal views, anterior to the top. (A', B, B') Lateral views, anterior left. (B', C') Enlarged views of boxed regions in B and C, respectively. Scale bars, 100 µm. (D-F) Fluorescent double-label WISH for (D) *rln3a* and *gsc2*, (E) *rln3a* and *nmbb*, and (F) *rln3a* and *cckb*. Dorsal views of 6 dpf larvae, anterior to the top. Z-projections. Scale bar, 10 µm. (G) Schematic depicting distribution of neuronal subtypes in the nucelus incertus (NI) of larval zebrafish. Green dots, *gsc2* expression; purple dots, *rln3a*

expression; blue dots, *nmbb* expression; pink dots and shading, *cckb* expression. IPN: interpeduncular nucleus, PAG: periaqueductal grey, NI: nucleus incertus.

Figure 1-1. Subset of neuropeptides expressed in NI of larval zebrafish. WISH for (A-A') *ccka*, (B-B') *cckb*, (C-C') *nmba*, (D-D') *nmbb* and (E-E') *nts* expression in 6 dpf larvae. Dorsal views of the same larvae were imaged at (A, B, C, D, E) dorsal and (A', B', C', D', E') ventral planes, anterior to the top. White arrowheads indicate the NI. Scale bar, 100 µm.

Figure 1-2. Partially overlapping expression of *rln3a* and *nmbb* in the zebrafish NI. Fluorescent double-label WISH for *rln3a* and *nmbb* transcripts. Dorsal views of 6 dpf larvae, anterior to the top. (A) Z-projection and (A'-A''') higher magnification image of NI from larva in A. (B-C'') NI in two additional larvae. (A'-C'') Optical sections showing neurons expressing (A', B, C) *rln3a*, (A'', B', C') *nmbb* and (A''', B'', C'') composite images. White arrowheads indicate neurons that co-express both genes. (A) Scale bar, 100 µm. (A'-C'') Scale bar, 10 µm. PAG: periaqueductal grey, NI: nucleus incertus.

Figure 2. Transgenic driver lines recapitulate *gsc2* and *rln3a* expression patterns. (A, D) CRISPR/Cas9 genome editing strategies used to generate (A) *Tg(gsc2:QF2)*^{c721} and (D) *Tg(rln3a:QF2, he1.1:YFP)*^{c836} driver lines. (B, C, E, F) Dorsal views of 6 dpf larvae, anterior to the top. (B, E) WISH for (B) *gsc2* and (E) *rln3a*. (C, F) Confocal Z-projections of (C) *Tg(gsc2:QF2)*^{c721}; *Tg(QUAS:GFP)*^{c578} and (F) *Tg(rln3a:QF2, he1.1:YFP)*^{c836}; *Tg(QUAS:GFP)*^{c578} larvae. Scale bars, 100 µm. sgRNA: single guide

RNA, *hsp70*: *heat shock cognate 70-kd protein, tandem duplicate 1* promoter, 5' UTR: 5' untranslated region, HA: homology arm, *he1.1*: promoter of hatching enzyme gene.

Figure 2-1. *QF2* driver lines recapitulate *gsc2* and *rln3a* expression patterns in the adult brain.

Drawing of adult zebrafish brain in lateral view (after Wullimann et al., 1996), indicating positions of coronal sections (70 µm) shown in (B-G). (B, D, F) WISH for (B) *gsc2* and (D, F) *rln3a*. (C, E, G) Confocal Z-projections of labeled neurons in (C) *Tg(gsc2:QF2)*^{c721}; *Tg(QUAS:GFP)*^{c578} and (E, G) *Tg(rln3a:QF2, he1.1:YFP)*^{c836}; *Tg(QUAS:GFP)*^{c578} brains. Anterior to the top. Dashed lines delineate ventricles and medial longitudinal fascicles (MLF). Scale bars, 100 µm. Ob: olfactory bulb, Tel: telencephalon, Hb: habenula, OT: optic tectum, IPN: interpeduncular nucleus, Ce: cerebellum, Md: medulla.

Figure 2-2. *gsc2* neurons reside outside the IPN in the adult brain.

Drawing of adult zebrafish brain in lateral view (after Wullimann et al., 1996), indicating positions of sections shown in (B-D'). (B-D') Two confocal optical sections are shown for each of three 70 µm vibratome slices from a representative *TgBAC(gng8:Eco.NfsB-2A-CAAX-GFP)*^{c375}; *Tg(gsc2:QF2)*^{c721}; *Tg(QUAS:NLS-mApple)*^{c718} adult brain. Sections are ordered from rostral to caudal with anterior to the top. Dashed lines delineate ventricles and the medial longitudinal fascicles (MLF). Arrowheads indicate mApple labeling of *gsc2* neuronal projections to the hypothalamus in B and B' and *gsc2* cell bodies in C-D.

Scale bar, 100 µm. Ob: olfactory bulb, Tel: telencephalon, Hb: habenula, OT: optic tectum, IPN: interpeduncular nucleus, Ce: cerebellum, Md: medulla.

Figure 3. *rln3a* and *gsc2* NI neurons are largely GABAergic.

(A-F'') Confocal images of 6 dpf larvae. (A-C) Lateral views, anterior left. (D-F'') Dorsal views, anterior to the top. (A) Z-projection of *Tg(gsc2:QF2)*^{c721}; *Tg(QUAS:GFP)*^{c578}; *Tg(slc17a6b:DsRed)*^{nns9Tg} larva. (B-F'') Optical sections. (B) PAG and (C) NI of a *Tg(rln3a:QF2, he1.1:YFP)*^{c836}; *Tg(QUAS:mApple, he1.1:CFP)*^{c788}; *Tg(slc17a6b:GFP)*^{zf139Tg} larva. (D) *Tg(gsc2:QF2)*^{c721}; *Tg(QUAS:mApple-CAAX, he1.1:mCherry)*^{c636}; *Tg(gad1b:GFP)*^{nn25Tg} larva. (D') Magnified view of boxed region in D. White arrowhead indicates a *Gad1b*-positive *gsc2*-positive neuron. (E-F'') *Tg(rln3a:QF2, he1.1:YFP)*^{c836}; *Tg(QUAS:mApple, he1.1:CFP)*^{c788}; *Tg(gad1b:GFP)*^{nn25Tg} larva. (E-E'') View of PAG. (F-F'') View of NI. (E', F') Magnified views of boxed regions in E and F. (E'', F'') Individual neurons indicated by arrowheads in E' and F' respectively. Top panels: GABAergic, middle panels: *rln3a*, bottom panels: composite. (G) Boxplot showing the percentage of *gsc2* and *rln3a* NI neurons, and *rln3a* PAG neurons that express *Tg(gad1b:GFP)*^{nn25Tg}, n = 3 larvae. Scale bars, 100 µm.

Figure 4. *gsc2* and *rln3a* neurons distinct projection patterns.

(A-J) Confocal optical sections of (A-E) *Tg(gng8:Eco.NfsB-2A-CAAX-GFP)*^{c375}; Tg*(gsc2:QF2)*^{c721}; *Tg(QUAS:mApple-CAAX, he1.1:mCherry)*^{c636} and (F-J) *Tg(gng8:Eco.NfsB-2A-CAAX-GFP)*^{c375}; *Tg(rln3a:QF2, he1.1:YFP)*^{c836}; *Tg(QUAS:mApple-CAAX, he1.1:mCherry)*^{c636} 6 dpf larvae ordered from dorsal to

ventral. (K-M) 3D reconstructions of confocal Z-stacks generated using Zen software (Zeiss), *Tg(rln3a:QF2, he1.1:YFP)*^{c836}; *Tg(QUAS:GFP-CAAX)*^{c591}; *Tg(QUAS:NLS-GFP, he1.1:CFP)*^{c682} larvae at 7 dpf showing efferents from (K) intact *rln3a* PAG (asterisks) and NI (arrows) neurons or following two-photon laser-mediated ablation of (L) PAG or (M) NI *rln3a* cell bodies at 6 dpf. Dorsal views, anterior to the top. Scale bars, 100 µm. NI: nucleus incertus, OT: optic tectum, CB: cerebellum, PC: posterior commissure, PAG: periaqueductal grey, MO: medulla oblongata, DI: diencephalon, IPN: interpeduncular nucleus, TEL: telencephalon, RH: rostral hypothalamus, LH: lateral hypothalamus, CH: caudal hypothalamus, PO: pre-optic area.

Movie 4-1. Axonal projections of *gsc2* neurons.

Rotating 3D reconstruction of a 6 dpf *Tg(gng8:Eco.NfsB-2A-CAAX-GFP)*^{c375}; Tg*(gsc2:QF2)*^{c721}; *Tg(QUAS:mApple-CAAX, he1.1:mCherry)*^{c636} larva generated using a Zeiss LSM 980 and Zen software. Hb-IPN pathway, green; *gsc2* neurons, magenta. Anterior to the top.

Movie 4-2. Axonal projections of *rln3a* neurons.

Rotating 3D reconstruction of a 6 dpf *Tg(gng8:Eco.NfsB-2A-CAAX-GFP)*^{c375}; *Tg(rln3a:QF2, he1.1:YFP)*^{c836}; *Tg(QUAS:mApple-CAAX, he1.1:mCherry)*^{c636} larva generated using a Zeiss LSM 980 and Zen software. Hb-IPN pathway, green; *rln3a* neurons, magenta. Anterior to the top.

Movie 4-3. Axonal projections of *rln3a* neurons after ablation of *rln3a* PAG cell bodies. Rotating 3D reconstruction of a 7 dpf *Tg(rln3a:QF2, he1.1:YFP)*^{c836}; *Tg(QUAS:GFP-CAAX)*^{c591}; *Tg(QUAS:NLS-GFP, he1.1:CFP)*^{c682} larva whose *rln3a* PAG neurons were ablated at 6 dpf reveals projections from the *rln3a* NI neurons to the IPN. Generated using a Zeiss LSM 980 and Zen software. *rln3a* neurons and projections, green. Anterior to the top.

Figure 5. *gsc2* and *rln3a* NI neurons innervate different dorsoventral IPN regions. (A-H') Confocal images of 6 dpf larvae. (A-B, E-F') *TgBAC(gng8:Eco.NfsB-2A-CAAX-GFP)*^{c375} and *Tg(gsc2:QF2)*^{c721} driving (A, A') *Tg(QUAS:NLS-mApple, he1.1:CFP)*^{c718} or (B, E-F') *Tg(QUAS:mApple-CAAX, he1.1:mCherry)*^{c636}. (C-D, G-H') *TgBAC*(*gng8:GAL4FF*)^{c426}*; Tg(UAS-E1B:NTR-mCherry)*^{c264} and *Tg(rln3a:QF2, he1.1:YFP)*^{c836} driving (C, C') *Tg(QUAS:NLS-GFP, he1.1:CFP)*^{c682} or (D, G-H') *Tg(QUAS:NLS-GFP, he1.1:CFP)*^{c682} and *Tg(QUAS:GFP-CAAX)*^{c591}. (A', C') Higher magnification images of larvae in A and C, respectively. (A, A', C, C') Z-projections. (B, D) optical sections. (A-D) Lateral views, anterior left. (E-H') Dorsal views, anterior to the top. Optical sections at the level of the (E, E', G, G') dorsal IPN or (F, F', H, H') ventral IPN of the same larvae. (E', F', G', H') Labeled efferent projections only. (I, J) Confocal Z-projections of coronal sections (70 µm) through adult brains of (I) *Tg(gsc2:QF2)*^{c721}; *Tg(QUAS:GFP-CAAX; he1.1:YFP)*^{c631} or (J) *Tg(rln3a:QF2; he1.1:YFP)*^{c836}; *Tg(QUAS:GFP-CAAX)*^{c591} fish. Anterior to the top. (K) Schematic of the IPN showing distinct dorsoventral regions innervated by *rln3a* and *gsc2* neurons. Scale bars, 100 µm. dIPN: dorsal IPN, vIPN: ventral IPN.

Figure 6. Increased calcium signaling in *gsc2* neurons upon optogenetic activation of the dHb.

Calcium transients were imaged at 2.6 Hz before, during, and after illumination with 561 nm light in 7 dpf larvae. (A) Drawings depicting imaging of calcium transients and optogenetic activation using confocal microscopy. (B-C') Representative maximum intensity projections of *GcaMP7a* fluorescence in (B) dHb and (B') *gsc2* neurons of the same larva, or (C) dHb and (C') *rln3a* NI neurons of the same larva. Anterior to the top. Scale bar, 100 µm. (D-E'') *Tg(gsc2:QF2)*^{c721} or (F-H'') *Tg(rln3a:QF2, he1.1:YFP)*^{c836} driver lines in (D-H) *TgBAC*(*gng8:GAL4FF*)^{c426}*; Tg(UAS:GcaMP7a)*^{zf415}; *Tg(QUAS:GcaMP7a)*^{c594} larvae (D, E, F, G, H) with or (D', E', F', G', H') without *Tg(UAS:ReaChR-RFP)*^{jf50}. The average change in GcaMP7a signaling (%ΔF/F) is shown for (D, D', F, F') the dorsal habenulae, (E, E') *gsc2* neurons, (G, G') *rln3a* NI neurons, and (H, H') *rln3a* PAG neurons. Shading indicates standard deviation. Gaps at light onset and offset are due to latency in switching the laser configuration. (D'', E'', F'', G'', H'') Average F_{post}/F_{pre} is shown for (D'', F'') the dHb, (E'') *gsc2* neurons, (G'') *rln3a* NI neurons, and (H'') *rln3a* PAG neurons of *ReaChR*$^{+}$ and *ReaChR*$^{-}$ larvae. F_{post} is the area under the curve for 15 frames (5.8 s) during 561 nm illumination and F_{pre} is the area under the curve for 15 frames (5.8 s) preceding 561 nm illumination. (D'', E'', F'', G'', H'') Black bars indicate mean ratios: (D'') 0.75 ± 0.15, n = 6 *ReaChR*$^{-}$ larvae, 2.95 ± 0.41, n = 5 *ReaChR*$^{+}$ larvae, ***p = 0.0004. (E'') 1.07 ± 0.15, n = 6 *ReaChR*$^{-}$ larvae, 1.86 ± 0.17, n = 5 *ReaChR*$^{+}$ larvae, **p = 0.0073. (F'') 1.22 ± 0.29, n = 5 *ReaChR*$^{-}$ larvae, 11.08 ± 6.54, n = 5 *ReaChR*$^{+}$ larvae, *p = 0.032. (G'') 1.82 ± 0.32, n = 5 *ReaChR*$^{-}$ larvae, 1.97 ± 0.59, n = 5 *ReaChR*$^{+}$ larvae, p = 0.83. (H'') 2.13 ± 0.27, n = 5 *ReaChR*$^{-}$

larvae, 1.83 ± 0.27, n = 5 *ReaChR*$^{+}$ larvae, p = 0.45. Extended y-axis in F'' to display higher values.

Figure 6-1. Calcium signaling in individual larvae and neurons.

Examples of calcium transients recorded from (A, B, D, E, G, H, J, K, M, O) individual larvae and from (C, F, I, L, N, P) single neurons in additional larvae. Calcium signaling was imaged at 2.6 Hz before, during, and after illumination with 561 nm light in 7 dpf larvae. GCaMP7a signaling (%ΔF/F) is shown for (A, D, G, J) the dorsal habenulae, (B, C, E, F) *gsc2* neurons, (H, I, K, L) *rln3a* NI neurons, and (M, N, O, P) *rln3a* PAG neurons. Shading indicates standard deviation. Gaps at light onset and offset are due to latency in switching the laser configuration. (A-F) *Tg(gsc2:QF2)*^{c721} or (G-P) *Tg(rln3a:QF2, he1.1:YFP)*^{c836} driver lines together with *TgBAC*(*gng8:GAL4FF*)^{c426}; *Tg(UAS:GCaMP7a)*^{zf415}; *Tg(QUAS:GCaMP7a)*^{c594} with (red trace) or without (green trace) *Tg(UAS:ReaChR-RFP)*^{if50}.

Figure 7. *gsc2* and *rln3a* NI neurons differ in their spontaneous activity and response to an aversive cue.

Calcium transients were imaged at 5.2 Hz in 7dpf larvae during a mild electric shock (25 V, 200 ms duration). (A) Drawing depicting delivery of shock to an immobilized larva during imaging. (B, C) Examples of maximum intensity projections for NI neurons in (B) *Tg(gsc2:QF2)*^{c721}; *Tg(QUAS:GCaMP7a)*^{c594} or (C) *Tg(rln3a:QF2, he1.1:YFP)*^{c836}; *Tg(QUAS:GCaMP7a)*^{c594} larvae. Dorsal views, anterior to the top. Scale bars, 10 μm. (D, E) *GCaMP7a* signaling (%ΔF/F) for representative individual (D) *gsc2* or (E) *rln3a*

neurons. Arrows indicate local maxima identified as peaks by the MATLAB *findpeaks* function (MinPeakProminence: 0.3, MinPeakWidth: 10). (D', E') Average %ΔF/F for all recorded (D') *gsc2* neurons (93 from 11 larvae) or (E') *rln3a* neurons (76 from 10 larvae). Shading indicates standard deviation. (F, F', G, G') Histogram of %ΔF/F amplitudes for (F, F') *gsc2* or (G, G') *rln3a* neurons during the (F, G) pre-shock or (F', G') post-shock period. (H, I) Average (H) number of peaks during the recording period (as depicted by arrows in examples D and E) and average (I) length of response for *gsc2* neurons and *rln3a* neurons, defined as the time required for the %ΔF/F to return to a value equal to or less than the average %ΔF/F in the 100 frames (18.9 seconds) prior to shock. Black bars in (H) indicate mean peaks for *gsc2* neurons (5.56 ± 0.63, n = 11 larvae) and *rln3a* neurons (9.91 ± 1.18, n = 10 larvae), **p = 0.0035. Black bars in (I) indicate mean response times for *gsc2* neurons (36.21 ± 8.42, n= 11 larvae) and *rln3a* neurons (10.63 ± 3.27, n= 10 larvae) *p = 0.045.

Movie 7-1. Response of *gsc2* neurons to shock.

Calcium signaling in the *gsc2* neurons of a 7 dpf *Tg(gsc2:QF2)*^{c721}; *Tg(QUAS:GCaMP7a)*^{c594} larva during the delivery of an electric shock (25 V, 200 ms duration), which is denoted by text in upper left corner. Calcium transients imaged at 5.2 Hz. Video sped up 3X.

Movie 7-2. Response of *rln3a* neurons to shock.

Calcium signaling in the *rln3a* neurons in the NI of a 7 dpf *Tg(rln3a:QF2, he1.1:YFP)*^{c836}; *Tg(QUAS:GCaMP7a)*^{c594} larva during the delivery of an electric shock (25 V, 200 ms

duration), which is denoted by text in upper left corner. Calcium transients imaged at 5.2 Hz. Video sped up 3X.

Figure 8. Loss of *rln3a* NI neurons increases spontaneous locomotor activity. (A-C’’’) Single optical sections from two-photon imaging of 6 dpf (A, A’) *Tg(gsc2:QF2)*^{c721}; *Tg(QUAS:GFP)*^{c578} or (B-C’’’) *Tg(rln3a:QF2, he1.1:YFP)*^{c836}; *Tg(QUAS:GFP)*^{c578} larvae (A, B, C, C’’) before and (A’, B’, C’, C’’’) after laser-mediated ablation of (A, A’) *gsc2* neurons, (B, B’) *rln3a* NI neurons, or (C, C’) left and (C’’, C’’’) right *rln3a* PAG neurons. Dorsal views, anterior to the top. Scale bars, 10 µm. (D-D’’’) Average locomotor activity during 5 seconds prior to and after shock. Shock delivery is denoted by the gray line. (E) Mean of total distance traveled during 5 seconds pre- and post-shock for unablated controls (pre = 0.86 ± 0.23 cm, post = 5.89 ± 0.64 cm, n = 27), or larvae with ablated *gsc2* (pre = 1.19 ± 0.31, post = 7.23 ± 1.20 cm, n = 17) *rln3a* NI (pre = 1.30 ± 0.26 cm, post = 8.09 ± 1.45 cm, n = 15), or *rln3a* PAG (pre = 0.72 ± 0.23 cm, post = 6.92 ± 1.07 cm, n = 17) neurons. Kruskal-Wallis rank sum test: ***$p = 2.2 \times 10^{-16}$. Dunn’s post-hoc tests with adjustment for multiple comparisons show no statistically significant differences within pre- and post-shock epochs, $p < 0.001$*** for each pre-shock vs. post-shock comparison. Unablated control group includes *Tg(gsc2:QF2)*^{c721}; *Tg(QUAS:GFP)*^{c578} and *Tg(rln3a:QF2, he1.1:YFP)*^{c836}; *Tg(QUAS:GFP)*^{c578} siblings of ablated larvae. (F-F’’’) Representative trajectories of 7 dpf larvae with ablated (F’) *gsc2* (F’’) *rln3a* NI or (F’’’) *rln3a* PAG neurons, and (F) sibling controls during the first 115 seconds of the recording (baseline activity). (G) Mean of distance traveled during the first 115 seconds of the recording for unablated controls

(19.87 ± 3.19 cm) or larvae with ablated *gsc2* (17.87 ± 3.84193 cm), *rln3a* NI (42.80 ± 5.27 cm,) or *rln3a* PAG (15.73 ± 3.55 cm) neurons. Kruskal-Wallis rank sum test: ***p = 0.00099. Dunn's post-hoc tests with adjustment for multiple comparisons show ablated *rln3a* NI neurons vs. unablated **p = 0.0019, ablated *rln3a* vs. *gsc2* NI neurons **p = 0.0019, or ablated *rln3a* NI vs. *rln3a* PAG neurons **p = 0.0019. (H) Average length of movement phases during the pre-shock period, defined as continuous phases of movement with no more than one second of prolonged immobility, for unablated controls (7.35 ± 1.34 seconds) or larvae with ablated *gsc2* (6.18 ± 1.14 seconds), *rln3a* NI (10.38 ± 1.17 seconds) or *rln3a* PAG (4.23 ± 0.74 seconds) neurons. Kruskal-Wallis rank sum test: **p = 0.0013. Dunn's post-hoc tests with adjustment for multiple comparisons show ablated *rln3a* NI neurons vs. unablated *p = 0.039, ablated *rln3a* vs. *gsc2* NI neurons ablated *p = 0.039, or ablated *rln3a* NI vs. *rln3a* PAG neurons ***p = 0.00055. (I) Mean number of phases of movement during the pre-shock period for unablated controls (7.74 ± 1.03) or larvae with ablated *gsc2* (6.88 ± 1.39), *rln3a* NI (8.13 ± 1.05), or *rln3a* PAG (7.41± 1.33) neurons. Kruskal-Wallis rank sum test: p = 0.89.

Figure 8-1. Confirmation of selective ablation of NI neuronal clusters.

(A-D') WISH for (A, A', C, C') *gsc2* or (B, B', D, D') *rln3a* was performed on 7 dpf larvae. (A', B') *Tg(gsc2:QF2)*^{c721}; *Tg(QUAS:GFP)*^{c578} larvae whose *gsc2* neurons were ablated at 6 dpf. (C', D') *Tg(rln3a:QF2, he1.1:YFP)*^{c836}; *Tg(QUAS:GFP)*^{c578} larvae whose *rln3a* NI neurons were ablated at 6 dpf. (A, B, C, D) Unablated sibling controls for larvae in A', B', C' and D' respectively. (D,D') Higher background due to the longer incubation time

required to detect *rln3a* transcripts, which are reduced in *Tg(rln3a:QF2, he1.1:YFP)*^{c836} heterozygotes relative to wild type. Dorsal views, anterior to the top.

Movie 8-1. Increased swimming behavior upon loss of *rln3a* NI neurons.

Freely swimming 7 dpf larvae. Left: Unablated control larva. Right: Larva whose *rln3a* NI neurons were ablated at 6 dpf. Red dot marks the position of the larva for ease of tracking. Larvae were removed from 1x phenylthiourea at 6 dpf after two-photon ablation protocol to allow for the development of pigment, which increases visibility.

Figure 8-2. Loss of *rln3a* NI neurons increases turning behavior.

Ratio of the total size, in degrees, of all calculated angles during the first 115 seconds of the recording, divided by total distance traveled in millimeters. (A) Mean ratio for unablated controls (81.94 ± 12.85), or larvae with ablated *gsc2* (81.53 ± 15.81), *rln3a* NI (182.72 ± 15.29), or *rln3a* PAG (84.26 ± 16.70) neurons. Kruskal-Wallis rank sum test: ***p = 0.00017. Dunn's post-hoc tests with adjustment for multiple comparisons show ablated *rln3a* NI neurons vs. unablated ***p = 0.00038, ablated *rln3a* vs. *gsc2* NI neurons ***p = 0.00066, or ablated *rln3a* NI vs. *rln3a* PAG neurons ***p = 0.00066. (B, C) Unablated control group includes only (B) *Tg(gsc2:QF2)*^{c721}; *Tg(QUAS:GFP)*^{c578} or (C) *Tg(rln3a:QF2, he1.1:YFP)*^{c836}; *Tg(QUAS:GFP)*^{c578} siblings of ablated larvae. Mean ratios: (B) Unablated c721 = 66.93 ± 15.38. (C) Unablated c836 = 93.95 ± 19.50. All other groups have the same values as in A. (B) Kruskal-Wallis rank sum test: ***p = 0.000097. Dunn's post-hoc tests with adjustment for multiple comparisons show ablated *rln3a* NI neurons vs. unablated ***p = 0.00057, ablated *rln3a* vs. *gsc2* NI neurons ***p =

0.00059, or ablated *rln3a* NI vs. *rln3a* PAG neurons ***p = 0.00061. (C) Kruskal-Wallis rank sum test: ***p = 0.00045. Dunn's post-hoc tests with adjustment for multiple comparisons show ablated *rln3a* NI neurons vs. unablated **p = 0.0045, ablated *rln3a* vs. *gsc2* NI neurons **p = 0.001, or ablated *rln3a* NI vs. *rln3a* PAG neurons **p = 0.001.

Figure 8-3. Comparisons between ablated and unablated larvae with the same genotype.

Unablated control group only includes only *Tg(gsc2:QF2)*^{c721}; *Tg(QUAS:GFP)*^{c578} (A, C, D, E) or *Tg(rln3a:QF2, he1.1:YFP)*^{c836}; *Tg(QUAS:GFP)*^{c578} (B, F, G, H) siblings of ablated larvae. (A, B) Mean of distance traveled during 5 seconds pre- and post-shock. (A) Unablated c721: pre = 1.30 ± 0.46 cm, post = 5.80 ± 0.61 cm. (B) Unablated c836: pre = 0.51 ± 0.18 cm, post = 5.96 ± 1.07 cm. (C, F) Mean of distance traveled during the first 115 seconds of the recording. (C) Unablated c721 = 19.33 ± 4.59 cm. (F) Unablated c836 = 20.29 ± 4.55 cm. (D, G) Average length of phases of movement during the pre-shock period, defined as continuous phases of movement with no more than one second of prolonged immobility. (D) Unablated c721 = 8.28 ± 3.11 seconds. (G) Unablated c836 = 6.64 ± 1.07 seconds. (E, H) Mean number of phases of movement during the pre-shock period. (E) Unablated c721 = 8.17 ± 1.99. (H) Unablated c836 = 7.4 ± 1.30. All other groups have the same values as in Figure 8. (A, B) Kruskal-Wallis rank sum test: (A) ***p = 4.74×10^{-15}, (B) ***p = 2.85×10^{-16}. (A, B) Dunn's post-hoc tests with adjustment for multiple comparisons show no statistically significant differences within pre- and post-shock epochs, p < 0.001*** for each pre-shock vs. post-shock comparison. (C) Kruskal-Wallis rank sum test: **p = 0.0012. Dunn's post-hoc

tests with adjustment for multiple comparisons show ablated *rln3a* NI neurons vs. unablated *p = 0.012, ablated *rln3a* vs. *gsc2* NI neurons **p = 0.0023, or ablated *rln3a* NI vs. *rln3a* PAG neurons **p = 0.0023. (D) Kruskal-Wallis rank sum test: **p = 0.0018. Dunn's post-hoc tests with adjustment for multiple comparisons show ablated *rln3a* NI neurons vs. unablated p = 0.098, ablated *rln3a* vs. *gsc2* NI neurons ablated p = 0.060, or ablated *rln3a* NI vs. *rln3a* PAG neurons ***p = 0.00076. (F) Kruskal-Wallis rank sum test: **p = 0.0012. Dunn's post-hoc tests with adjustment for multiple comparisons show ablated *rln3a* NI neurons vs. unablated **p = 0.0078, ablated *rln3a* vs. *gsc2* NI neurons **p = 0.0022, or ablated *rln3a* NI vs. *rln3a* PAG neurons **p = 0.0022. (G) Kruskal-Wallis rank sum test: **p = 0.0012. Dunn's post-hoc tests with adjustment for multiple comparisons show ablated *rln3a* NI neurons vs. unablated p = 0.099, ablated *rln3a* vs. *gsc2* NI neurons ablated *p = 0.042, or ablated *rln3a* NI vs. *rln3a* PAG neurons ***p = 0.00049. (E, H) Kruskal-Wallis rank sum test: (E) p = 0.87, (H) p = 0.90.

Acknowledgements

We thank Dr. Bryan Luikart for sharing his expertise and equipment for two-photon microscopy, Jean-Michael Chanchu for generating *QUAS* transgenic lines, Essence Vinson and Ming Wu for assistance with RNA *in situ* hybridization, Dr. Jeffrey Mumm and Dr. Filippo Del Bene for providing plasmids, and Dr. Rejji Kuruvilla and Dr. Erik Duboué for valuable feedback on the manuscript. This work was supported by a National Science Foundation Graduate Research Fellowship DGE-1746891 (EDS) and by the National Institutes of Health under award R37HD091280 (MEH).

References

Agetsuma M, Aizawa H, Aoki T, Nakayama R, Takahoko M, Goto M, Sassa T, Amo R, Shiraki T, Kawakami K, Hosoya T, Higashijima S, Okamoto H (2010) The habenula is crucial for experience-dependent modification of fear responses in zebrafish. Nat Neurosci 13:1354–1356.

Albus M (1988) Cholecystokinin. Progress in Neuro-Psychopharmacology and Biological Psychiatry 12:S5–S21.

Argenton F, Zecchin E, Bortolussi M (1999) Early appearance of pancreatic hormone-expressing cells in the zebrafish embryo. Mechanisms of Development 87:217–221.

Auer TO, Duroure K, De Cian A, Concordet J-P, Del Bene F (2014) Highly efficient CRISPR/Cas9-mediated knock-in in zebrafish by homology-independent DNA repair. Genome Res 24:142–153.

Baraban SC (2013) Forebrain electrophysiological recording in larval zebrafish. J Vis Exp 50104.

Bittencourt JC, Sawchenko PE (2000) Do centrally administered neuropeptides access cognate receptors?: an analysis in the central corticotropin-releasing factor system. J Neurosci 20:1142–1156.

Burazin TCD, Bathgate RAD, Macris M, Layfield S, Gundlach AL, Tregear GW (2002) Restricted, but abundant, expression of the novel rat gene-3 (R3) relaxin in the dorsal tegmental region of brain. J Neurochem 82:1553–1557.

Choi J-H, Duboue ER, Macurak M, Chanchu J-M, Halpern ME (2021) Specialized neurons in the right habenula mediate response to aversive olfactory cues. eLife 10:e72345.

Chou M-Y, Amo R, Kinoshita M, Cherng B-W, Shimazaki H, Agetsuma M, Shiraki T, Aoki T, Takahoko M, Yamazaki M, Higashijima S, Okamoto H (2016) Social conflict resolution regulated by two dorsal habenular subregions in zebrafish. Science 352:87–90.

Concha ML, Wilson SW (2001) Asymmetry in the epithalamus of vertebrates. Journal of Anatomy 199:63–84.

Davison JM, Akitake CM, Goll MG, Rhee JM, Gosse N, Baier H, Halpern ME, Leach SD, Parsons MJ (2007) Transactivation from Gal4-VP16 transgenic insertions for tissue-specific cell labeling and ablation in zebrafish. Dev Biol 304:811–824.

deCarvalho TN, Akitake CM, Thisse C, Thisse B, Halpern ME (2013) Aversive cues fail to activate fos expression in the asymmetric olfactory-habenula pathway of zebrafish. Front Neural Circuits 7:98.

deCarvalho TN, Subedi A, Rock J, Harfe BD, Thisse C, Thisse B, Halpern ME, Hong E (2014) Neurotransmitter map of the asymmetric dorsal habenular nuclei of zebrafish. Genesis 52:636–655.

Doll CA, Burkart JT, Hope KD, Halpern ME, Gamse JT (2011) Subnuclear development of the zebrafish habenular nuclei requires ER translocon function. Dev Biol 360:44–57.

Donizetti A, Grossi M, Pariante P, D'Aniello E, Izzo G, Minucci S, Aniello F (2008) Two neuron clusters in the stem of postembryonic zebrafish brain specifically express relaxin-3 gene: first evidence of nucleus incertus in fish. Dev Dyn 237:3864–3869.

Dreosti E, Vendrell Llopis N, Carl M, Yaksi E, Wilson SW (2014) Left-right asymmetry is required for the habenulae to respond to both visual and olfactory stimuli. Curr Biol 24:440–445.

Duboué ER, Hong E, Eldred KC, Halpern ME (2017) Left Habenular Activity Attenuates Fear Responses in Larval Zebrafish. Curr Biol 27:2154-2162.e3.

Facchin L, Duboué ER, Halpern ME (2015) Disruption of Epithalamic Left-Right Asymmetry Increases Anxiety in Zebrafish. J Neurosci 35:15847–15859.

Farooq U, Kumar JR, Rajkumar R, Dawe GS (2016) Electrical microstimulation of the nucleus incertus induces forward locomotion and rotation in rats. Physiology & Behavior 160:50–58.

Funato H, Sato M, Sinton CM, Gautron L, Williams SC, Skach A, Elmquist JK, Skoultchi AI, Yanagisawa M (2010) Loss of Goosecoid-like and DiGeorge syndrome critical region 14 in interpeduncular nucleus results in altered regulation of rapid eye movement sleep. Proc Natl Acad Sci USA 107:18155–18160.

Furman DJ, Gotlib IH (2016) Habenula responses to potential and actual loss in major depression: preliminary evidence for lateralized dysfunction. Soc Cogn Affect Neurosci 11:843–851.

Gamse JT, Kuan Y-S, Macurak M, Brösamle C, Thisse B, Thisse C, Halpern ME (2005) Directional asymmetry of the zebrafish epithalamus guides dorsoventral innervation of the midbrain target. Development 132:4869–4881.

Goll MG, Anderson R, Stainier DYR, Spradling AC, Halpern ME (2009) Transcriptional silencing and reactivation in transgenic zebrafish. Genetics 182:747–755.

Gong S, Zheng C, Doughty ML, Losos K, Didkovsky N, Schambra UB, Nowak NJ, Joyner A, Leblanc G, Hatten ME, Heintz N (2003) A gene expression atlas of the central nervous system based on bacterial artificial chromosomes. Nature 425:917–925.

Goto M, Swanson LW, Canteras NS (2001) Connections of the nucleus incertus. J Comp Neurol 438:86–122.

Gottlieb S, Hanes SD, Golden JA, Oakey RJ, Budarf ML (1998) Goosecoid-like, a gene deleted in DiGeorge and velocardiofacial syndromes, recognizes DNA with a bicoid-like specificity and is expressed in the developing mouse brain. Hum Mol Genet 7:1497–1505.

Hadley Wickham (2016) ggplot2: Elegant Graphics for Data Analysis.

Harris JA, Guglielmotti V, Bentivoglio M (1996) Diencephalic asymmetries. Neurosci Biobehav Rev 20:637–643.

Hong E, Santhakumar K, Akitake CA, Ahn SJ, Thisse C, Thisse B, Wyart C, Mangin J-M, Halpern ME (2013) Cholinergic left-right asymmetry in the habenulo-interpeduncular pathway. Proc Natl Acad Sci USA 110:21171–21176.

Hosken IT, Sutton SW, Smith CM, Gundlach AL (2015) Relaxin-3 receptor (Rxfp3) gene knockout mice display reduced running wheel activity: Implications for role of relaxin-3/RXFP3 signalling in sustained arousal. Behavioural Brain Research 278:167–175.

Hwang WY, Fu Y, Reyon D, Maeder ML, Tsai SQ, Sander JD, Peterson RT, Yeh J-RJ, Joung JK (2013) Efficient genome editing in zebrafish using a CRISPR-Cas system. Nat Biotechnol 31:227–229.

Jao L-E, Wente SR, Chen W (2013) Efficient multiplex biallelic zebrafish genome editing using a CRISPR nuclease system. Proc Natl Acad Sci USA 110:13904–13909.

Jennes L, Stumpf WE, Kalivas PW (1982) Neurotensin: Topographical distribution in rat brain by immunohistochemistry. J Comp Neurol 210:211–224.

K M Masum Habib (2022) PlotPub - Publication Quality Graphs in MATLAB.

Kimura Y, Hisano Y, Kawahara A, Higashijima S (2014) Efficient generation of knock-in transgenic zebrafish carrying reporter/driver genes by CRISPR/Cas9-mediated genome engineering. Sci Rep 4:6545.

Kubota Y, Inagaki S, Shiosaka S, Cho HJ, Tateishi K, Hashimura E, Hamaoka T, Tohyama M (1983) The distribution of cholecystokinin octapeptide-like structures in the lower brain stem of the rat: An immunohistochemical analysis. Neuroscience 9:587–604.

Kwan KM, Fujimoto E, Grabher C, Mangum BD, Hardy ME, Campbell DS, Parant JM, Yost HJ, Kanki JP, Chien C-B (2007) The Tol2kit: a multisite gateway-based construction kit for Tol2 transposon transgenesis constructs. Dev Dyn 236:3088–3099.

Lawson RP, Nord CL, Seymour B, Thomas DL, Dayan P, Pilling S, Roiser JP (2017) Disrupted habenula function in major depression. Mol Psychiatry 22:202–208.

Lawther AJ, Clissold ML, Ma S, Kent S, Lowry CA, Gundlach AL, Hale MW (2015) Anxiogenic drug administration and elevated plus-maze exposure in rats activate populations of relaxin-3 neurons in the nucleus incertus and serotonergic neurons in the dorsal raphe nucleus. Neuroscience 303:270–284.

Liang JO, Etheridge A, Hantsoo L, Rubinstein AL, Nowak SJ, Izpisúa Belmonte JC, Halpern ME (2000) Asymmetric nodal signaling in the zebrafish diencephalon positions the pineal organ. Development 127:5101–5112.

Lin JY, Knutsen PM, Muller A, Kleinfeld D, Tsien RY (2013) ReaChR: a red-shifted variant of channelrhodopsin enables deep transcranial optogenetic excitation. Nat Neurosci 16:1499–1508.

Lu L, Ren Y, Yu T, Liu Z, Wang S, Tan L, Zeng J, Feng Q, Lin R, Liu Y, Guo Q, Luo M (2020) Control of locomotor speed, arousal, and hippocampal theta rhythms by the nucleus incertus. Nat Commun 11:262.

Ma S, Allocca G, Ong-Pålsson EKE, Singleton CE, Hawkes D, McDougall SJ, Williams SJ, Bathgate RAD, Gundlach AL (2017) Nucleus incertus promotes cortical desynchronization and behavioral arousal. Brain Struct Funct 222:515–537.

Ma S, Blasiak A, Olucha-Bordonau FE, Verberne AJM, Gundlach AL (2013) Heterogeneous responses of nucleus incertus neurons to corticotrophin-releasing factor and coherent activity with hippocampal theta rhythm in the rat. J Physiol 591:3981–4001.

Ma S, Bonaventure P, Ferraro T, Shen P-J, Burazin TCD, Bathgate R a. D, Liu C, Tregear GW, Sutton SW, Gundlach AL (2007) Relaxin-3 in GABA projection neurons of nucleus incertus suggests widespread influence on forebrain circuits via G-protein-coupled receptor-135 in the rat. Neuroscience 144:165–190.

Ma S, Gundlach AL (2015) Ascending Control of Arousal and Motivation: Role of Nucleus Incertus and its Peptide Neuromodulators in Behavioural Responses to Stress. J Neuroendocrinol 27:457–467.

Ma S, Olucha-Bordonau FE, Hossain MA, Lin F, Kuei C, Liu C, Wade JD, Sutton SW, Nuñez A, Gundlach AL (2009) Modulation of hippocampal theta oscillations and spatial memory by relaxin-3 neurons of the nucleus incertus. Learn Mem 16:730–742.

McLaughlin I, Dani JA, De Biasi M (2017) The medial habenula and interpeduncular nucleus circuitry is critical in addiction, anxiety, and mood regulation. J Neurochem 142 Suppl 2:130–143.

Miyasaka N, Morimoto K, Tsubokawa T, Higashijima S -i., Okamoto H, Yoshihara Y (2009) From the Olfactory Bulb to Higher Brain Centers: Genetic Visualization of Secondary Olfactory Pathways in Zebrafish. Journal of Neuroscience 29:4756–4767.

Muto A, Ohkura M, Abe G, Nakai J, Kawakami K (2013) Real-Time Visualization of Neuronal Activity during Perception. Current Biology 23:307–311.

Nasirova N, Quina LA, Morton G, Walker A, Turner EE (2020) Mapping Cell Types and Efferent Pathways in the Ascending Relaxin-3 System of the Nucleus Incertus. eNeuro 7:ENEURO.0272-20.2020.

Nuñez A, Cervera-Ferri A, Olucha-Bordonau F, Ruiz-Torner A, Teruel V (2006) Nucleus incertus contribution to hippocampal theta rhythm generation. European Journal of Neuroscience 23:2731–2738.

Ohki-Hamazaki H (2000) Neuromedin B. Progress in Neurobiology 62:297–312.

Olson I, Suryanarayana SM, Robertson B, Grillner S (2017) Griseum centrale, a homologue of the periaqueductal gray in the lamprey. IBRO Reports 2:24–30.

Olucha-Bordonau FE, Albert-Gascó H, Ros-Bernal F, Rytova V, Ong-Pålsson EKE, Ma S, Sánchez-Pérez AM, Gundlach AL (2018) Modulation of forebrain function by nucleus incertus and relaxin-3/RXFP3 signaling. CNS Neurosci Ther 24:694–702.

Olucha-Bordonau FE, Teruel V, Barcia-González J, Ruiz-Torner A, Valverde-Navarro AA, Martínez-Soriano F (2003) Cytoarchitecture and efferent projections of the nucleus incertus of the rat. J Comp Neurol 464:62–97.

Palva JM, Palva S (2012) Infra-slow fluctuations in electrophysiological recordings, blood-oxygenation-level-dependent signals, and psychophysical time series. NeuroImage 62:2201–2211.

Passerin AM, Cano G, Rabin BS, Delano BA, Napier JL, Sved AF (2000) Role of locus coeruleus in foot shock-evoked Fos expression in rat brain. Neuroscience 101:1071–1082.

Petrucco L, Lavian H, Wu YK, Svara F, Štih V, Portugues R (2023) Neural dynamics and architecture of the heading direction circuit in zebrafish. Nat Neurosci 26:765–773.

Potter CJ, Tasic B, Russler EV, Liang L, Luo L (2010) The Q System: A Repressible Binary System for Transgene Expression, Lineage Tracing, and Mosaic Analysis. Cell 141:536–548.

Potter E, Sutton S, Donaldson C, Chen R, Perrin M, Lewis K, Sawchenko PE, Vale W (1994) Distribution of corticotropin-releasing factor receptor mRNA expression in the rat brain and pituitary. Proc Natl Acad Sci USA 91:8777–8781.

R Core Team (n.d.) R: A language and environment for statistical computing.

Rajkumar R, Wu Y, Farooq U, Tan WH, Dawe GS (2016) Stress activates the nucleus incertus and modulates plasticity in the hippocampo-medial prefrontal cortical pathway. Brain Res Bull 120:83–89.

Ranft K, Dobrowolny H, Krell D, Bielau H, Bogerts B, Bernstein H-G (2010) Evidence for structural abnormalities of the human habenular complex in affective disorders but not in schizophrenia. Psychol Med 40:557–567.

Riabinina O, Potter CJ (2016) The Q-System: A Versatile Expression System for Drosophila. Methods Mol Biol 1478:53–78.

Ryan PJ, Büchler E, Shabanpoor F, Hossain MA, Wade JD, Lawrence AJ, Gundlach AL (2013) Central relaxin-3 receptor (RXFP3) activation decreases anxiety- and depressive-like behaviours in the rat. Behav Brain Res 244:142–151.

Ryczko D, Dubuc R (2017) Dopamine and the Brainstem Locomotor Networks: From Lamprey to Human. Front Neurosci 11:295.

Saint-Jore B, Puech A, Heyer J, Lin Q, Raine C, Kucherlapati R, Skoultchi AI (1998) Goosecoid-like (GSCL), a candidate gene for velocardiofacial syndrome, is not essential for normal mouse development. Human Molecular Genetics 7:1841–1849.

Satou C, Kimura Y, Hirata H, Suster ML, Kawakami K, Higashijima S (2013) Transgenic tools to characterize neuronal properties of discrete populations of zebrafish neurons. Development 140:3927–3931.

Savitz JB, Nugent AC, Bogers W, Roiser JP, Bain EE, Neumeister A, Zarate CA, Manji HK, Cannon DM, Marrett S, Henn F, Charney DS, Drevets WC (2011) Habenula volume in bipolar disorder and major depressive disorder: a high-resolution magnetic resonance imaging study. Biol Psychiatry 69:336–343.

Schindelin J, Arganda-Carreras I, Frise E, Kaynig V, Longair M, Pietzsch T, Preibisch S, Rueden C, Saalfeld S, Schmid B, Tinevez J-Y, White DJ, Hartenstein V, Eliceiri K, Tomancak P, Cardona A (2012) Fiji: an open-source platform for biological-image analysis. Nat Methods 9:676–682.

Severi KE, Portugues R, Marques JC, O'Malley DM, Orger MB, Engert F (2014) Neural control and modulation of swimming speed in the larval zebrafish. Neuron 83:692–707.

Smith CM, Hosken IT, Sutton SW, Lawrence AJ, Gundlach AL (2012) Relaxin-3 null mutation mice display a circadian hypoactivity phenotype. Genes, Brain and Behavior 11:94–104.

Smith CM, Ryan PJ, Hosken IT, Ma S, Gundlach AL (2011) Relaxin-3 systems in the brain--the first 10 years. J Chem Neuroanat 42:262–275.

Smith CM, Shen P-J, Banerjee A, Bonaventure P, Ma S, Bathgate RAD, Sutton SW, Gundlach AL (2010) Distribution of relaxin-3 and RXFP3 within arousal, stress, affective, and cognitive circuits of mouse brain. J Comp Neurol 518:4016–4045.

Streeter GL (1903) Anatomy of the floor of the fourth ventricle. (The relations between the surface markings and the underlying structures.). Am J Anat 2:299–313.

Subedi A, Macurak M, Gee ST, Monge E, Goll MG, Potter CJ, Parsons MJ, Halpern ME (2014) Adoption of the Q transcriptional regulatory system for zebrafish transgenesis. Methods 66:433–440.

Suster ML, Sumiyama K, Kawakami K (2009) Transposon-mediated BAC transgenesis in zebrafish and mice. BMC Genomics 10:477.

Szlaga A, Sambak P, Trenk A, Gugula A, Singleton CE, Drwiega G, Blasiak T, Ma S, Gundlach AL, Blasiak A (2022) Functional Neuroanatomy of the Rat Nucleus Incertus–Medial Septum Tract: Implications for the Cell-Specific Control of the Septohippocampal Pathway. Front Cell Neurosci 16:836116.

Szőnyi A, Sos KE, Nyilas R, Schlingloff D, Domonkos A, Takács VT, Pósfai B, Hegedüs P, Priestley JB, Gundlach AL, Gulyás AI, Varga V, Losonczy A, Freund TF, Nyiri G (2019) Brainstem nucleus incertus controls contextual memory formation. Science 364:eaaw0445.

Tanaka M, Iijima N, Miyamoto Y, Fukusumi S, Itoh Y, Ozawa H, Ibata Y (2005) Neurons expressing relaxin 3/INSL 7 in the nucleus incertus respond to stress. Eur J Neurosci 21:1659–1670.

Thirumalai V, Cline HT (2008) Endogenous Dopamine Suppresses Initiation of Swimming in Prefeeding Zebrafish Larvae. Journal of Neurophysiology 100:1635–1648.

Thisse C, Thisse B, Schilling TF, Postlethwait JH (1993) Structure of the zebrafish snail1 gene and its expression in wild-type, spadetail and no tail mutant embryos. Development 119:1203–1215.

Walker C (1998) Chapter 3 Haploid Screens and Gamma-Ray Mutagenesis In: Methods in Cell Biology , pp43–70. Elsevier.

Wee CL, Song EY, Johnson RE, Ailani D, Randlett O, Kim J-Y, Nikitchenko M, Bahl A, Yang C-T, Ahrens MB, Kawakami K, Engert F, Kunes S (2019) A bidirectional network for appetite control in larval zebrafish. Elife 8.

Wierson WA et al. (2020) Efficient targeted integration directed by short homology in zebrafish and mammalian cells. Elife 9.

Wullimann MF, Rupp B, Reichert H (1996) Neuroanatomy of the Zebrafish Brain. Basel: Birkhäuser Basel.

Xie X, Mathias JR, Smith M-A, Walker SL, Teng Y, Distel M, Köster RW, Sirotkin HI, Saxena MT, Mumm JS (2012) Silencer-delimited transgenesis: NRSE/RE1 sequences promote neural-specific transgene expression in a NRSF/REST-dependent manner. BMC Biol 10:93.

Zaupa M, Naini SMA, Younes MA, Bullier E, Duboué ER, Le Corronc H, Soula H, Wolf S, Candelier R, Legendre P, Halpern ME, Mangin J-M, Hong E (2021) Trans-inhibition of axon terminals underlies competition in the habenulo-interpeduncular pathway. Current Biology 31:4762-4772.e5.

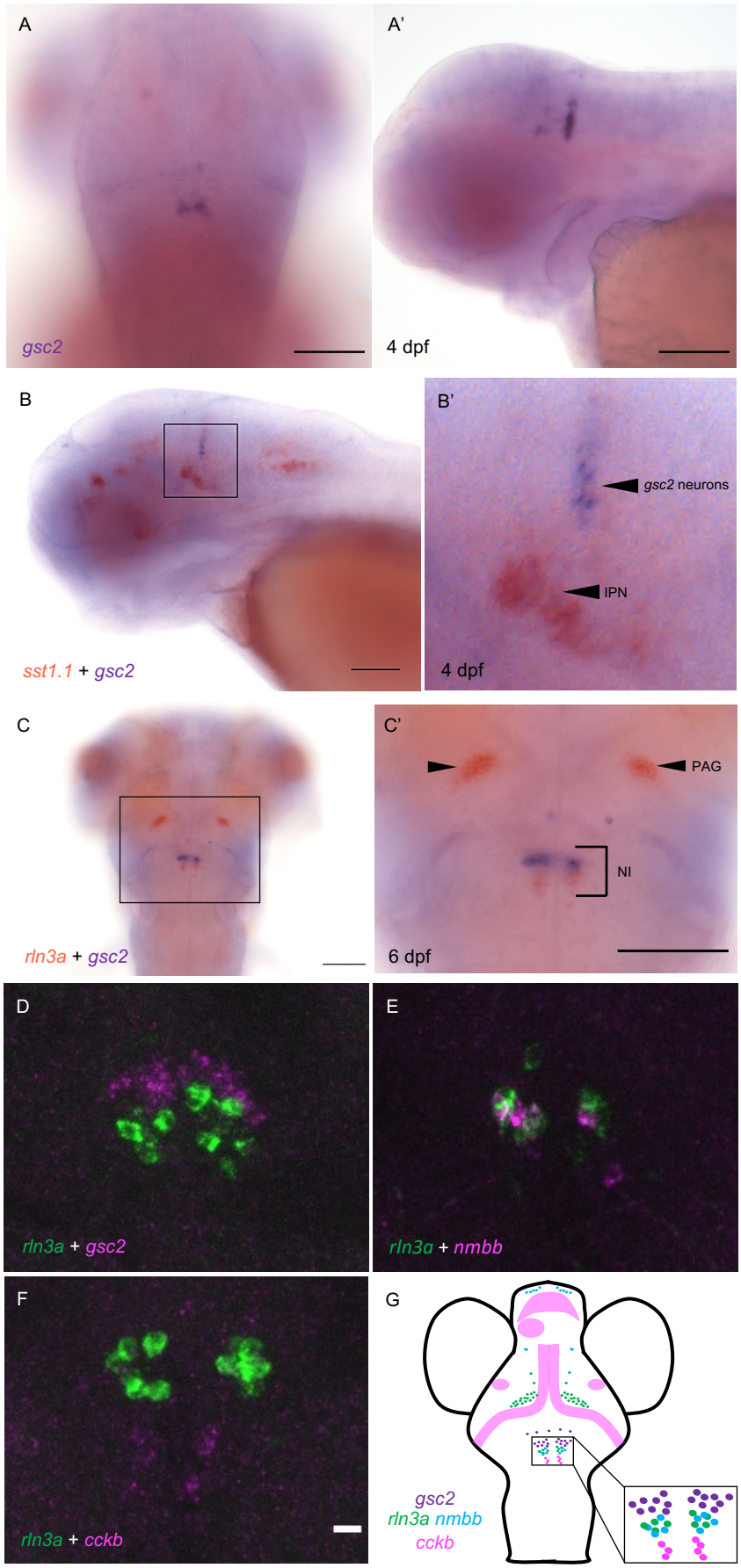
A
gsc2
A'
4 dpf
B
sst1.1 + gsc2
B'
gsc2 neurons
IPN
4 dpf
C
rln3a + gsc2
C'
PAG
NI
6 dpf
D
rln3a + gsc2
E
rln3a + nmbb
F
rln3a + cckb
G
gsc2
rln3a nmbb
cckb

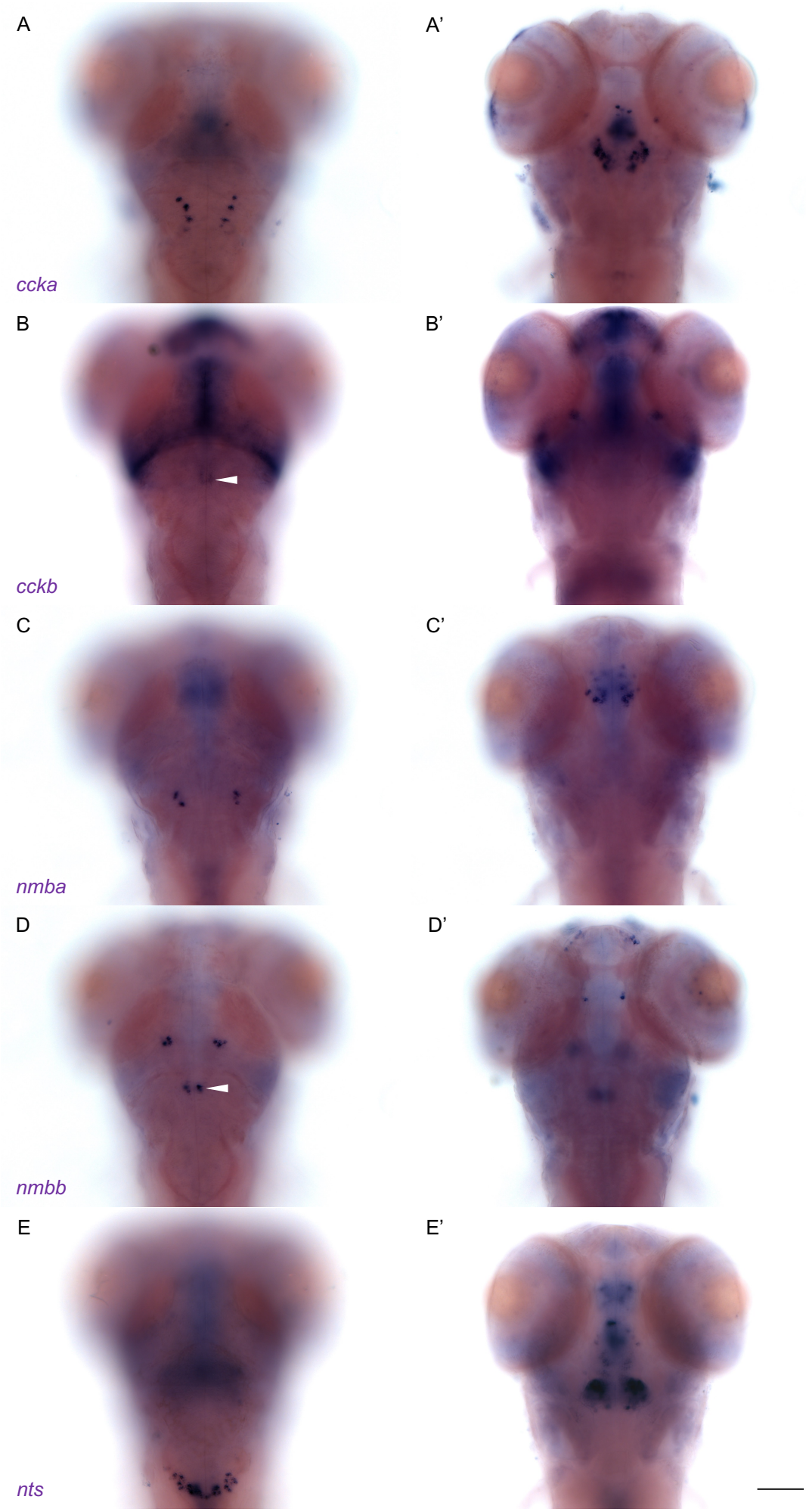
A
A'
cck a
B
B'
cckb
C
C'
nmba
D
D'
nmbb
E
E'
nts

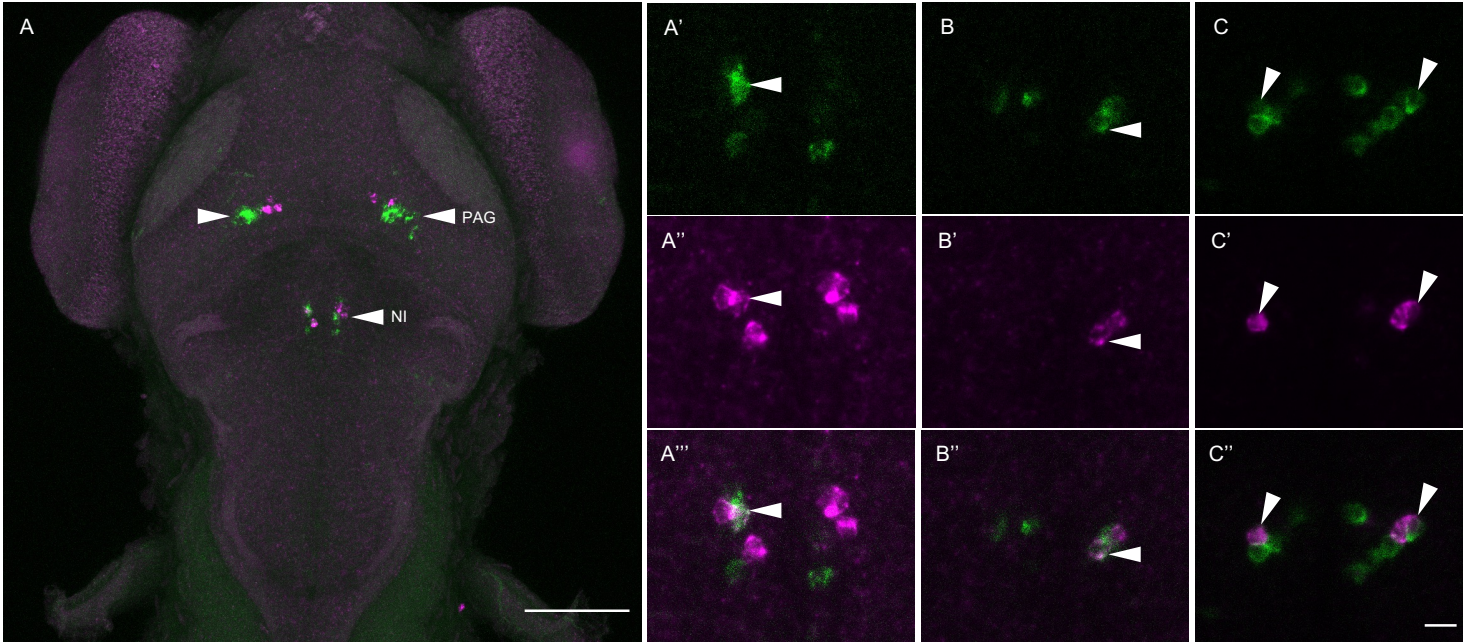

rln3a + *nmbb*

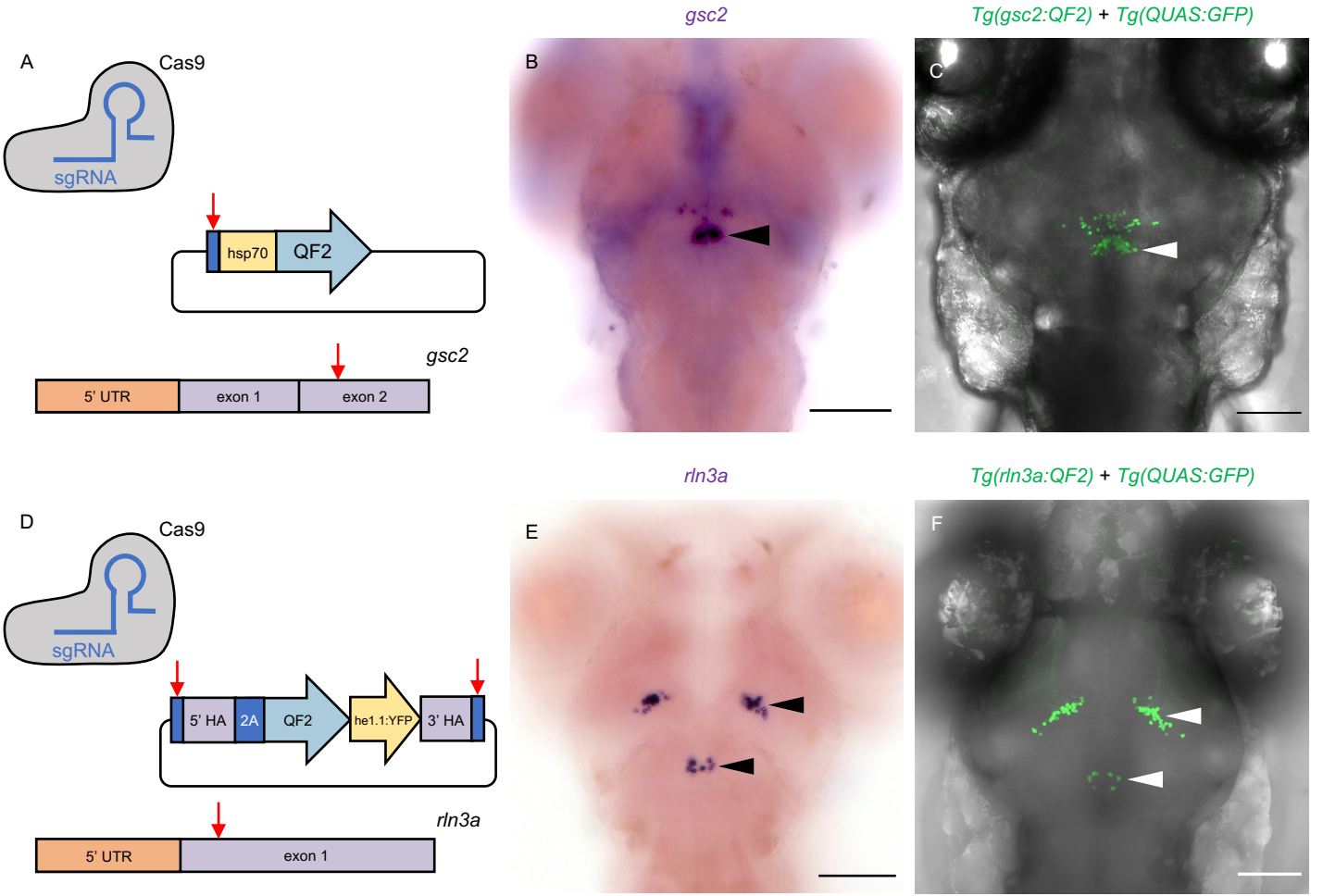
A
Cas9
sgRNA
hsp70
QF2
gsc2
5' UTR
exon 1
exon 2
gsc2
B
Tg(gsc2:QF2) + Tg(QUAS:GFP)
C
D
Cas9
sgRNA
5' HA
2A
QF2
he1.1:YFP
3' HA
rln3a
5' UTR
exon 1
rln3a
E
Tg(rln3a:QF2) + Tg(QUAS:GFP)
F

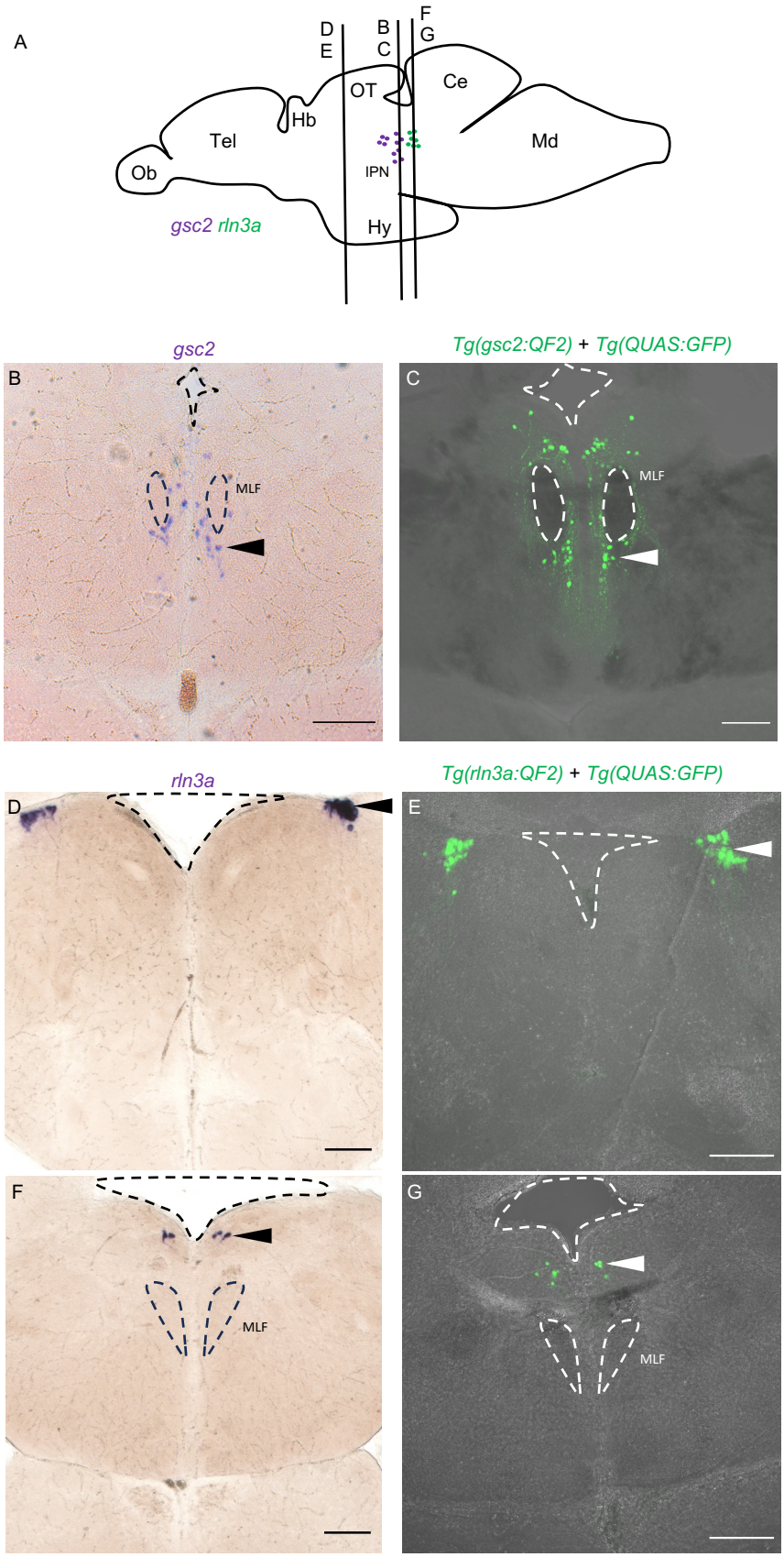
A
D
E
B
C
F
G
OT
Ce
Hb
Tel
Md
Ob
IPN
gsc2 rln3a
Hy
gsc2
Tg(gsc2:QF2) + Tg(QUAS:GFP)
B
C
MLF
MLF
rln3a
Tg(rln3a:QF2) + Tg(QUAS:GFP)
D
E
F
G
MLF
MLF

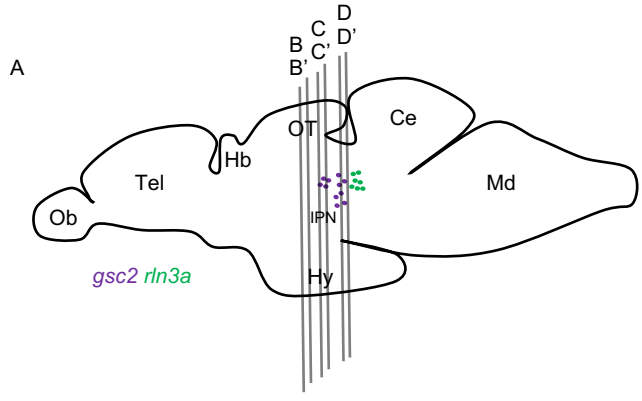

TgBAC(gng8:Eco.NfsB-2A-CAAX-GFP) +
Tg(gsc2:QF2) + *Tg(QUAS:NLS-mApple)*

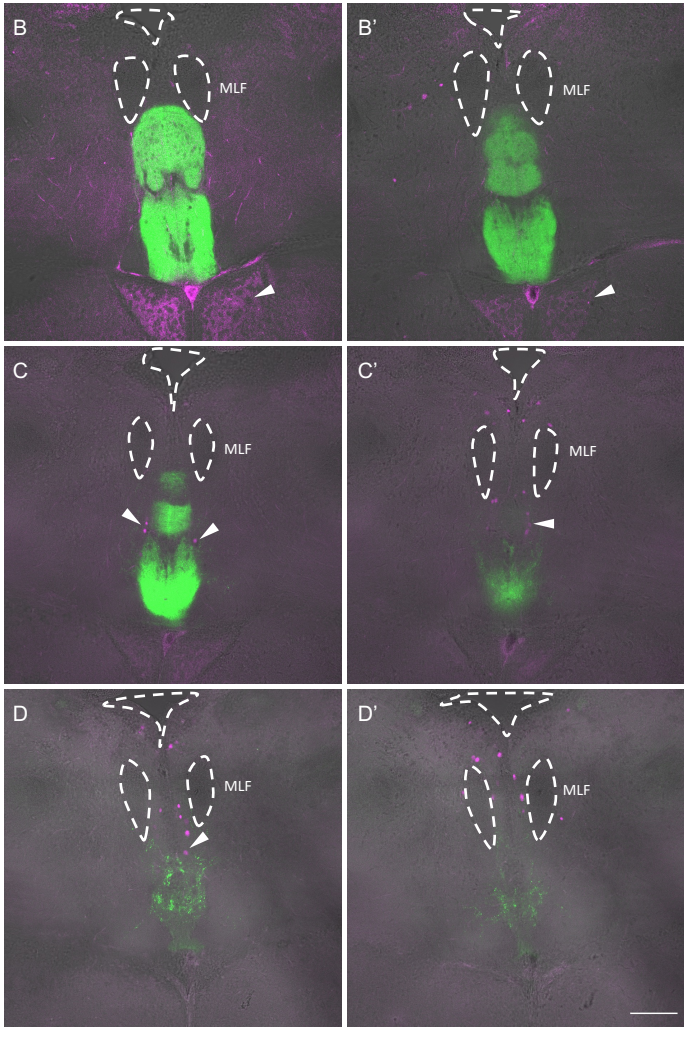

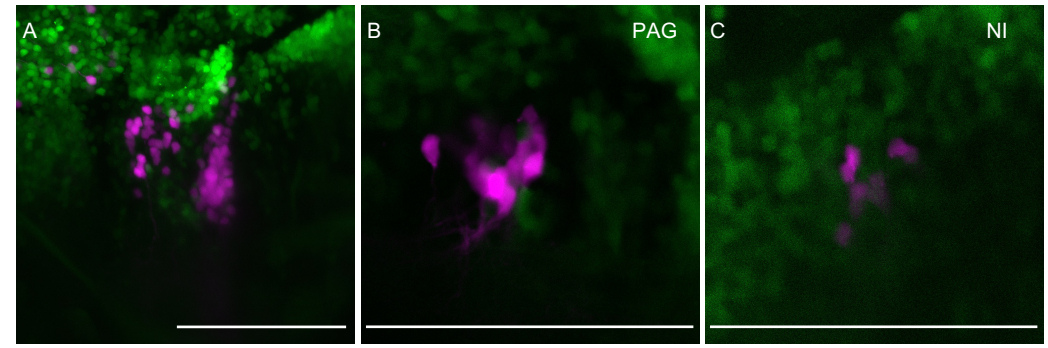

glutamatergic neurons + *gsc2* neurons

glutamatergic neurons + *rln3a* neurons

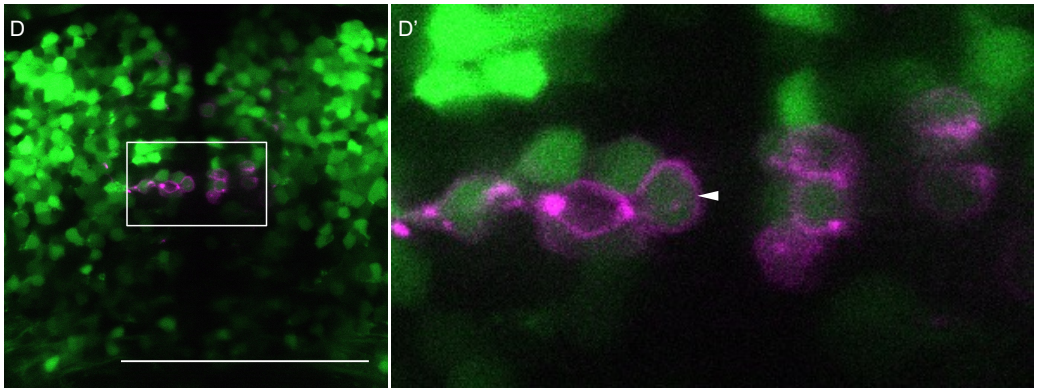

GABAerigc neurons + *gsc2* neurons

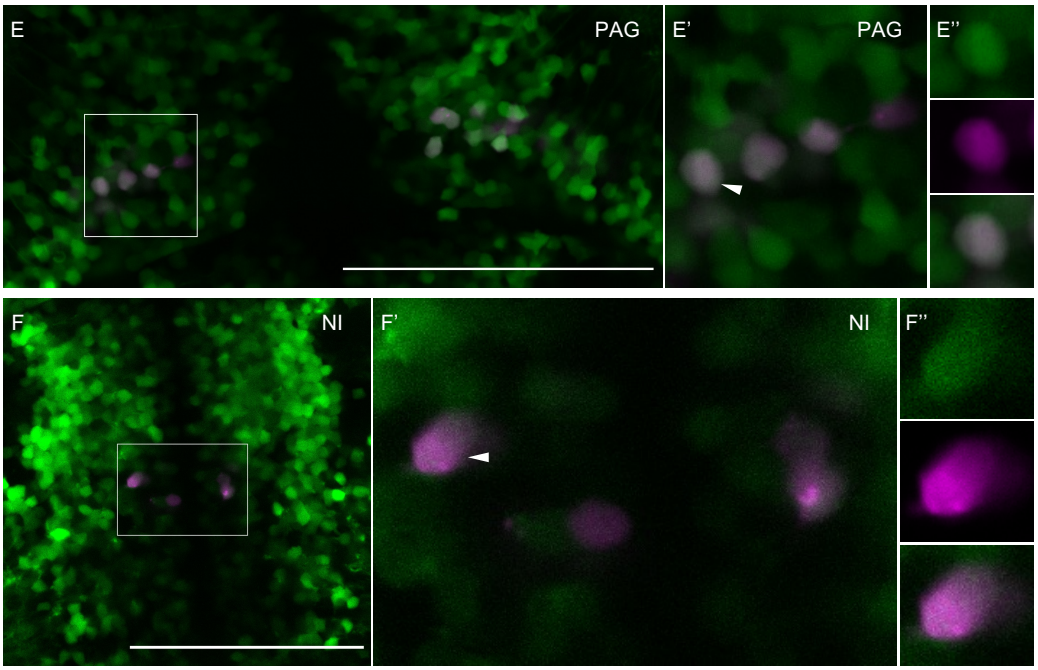

GABAerigc neurons + *rln3a* neurons

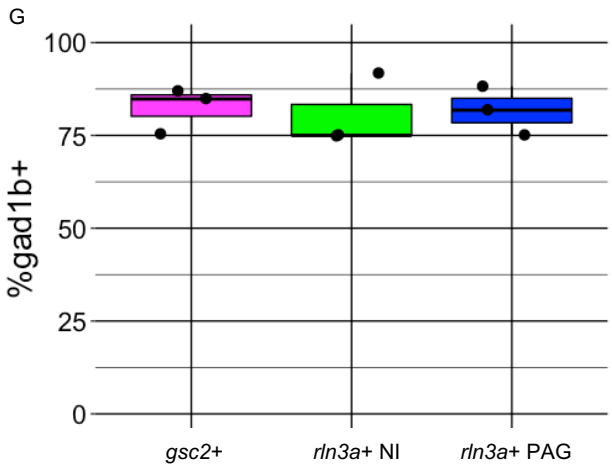

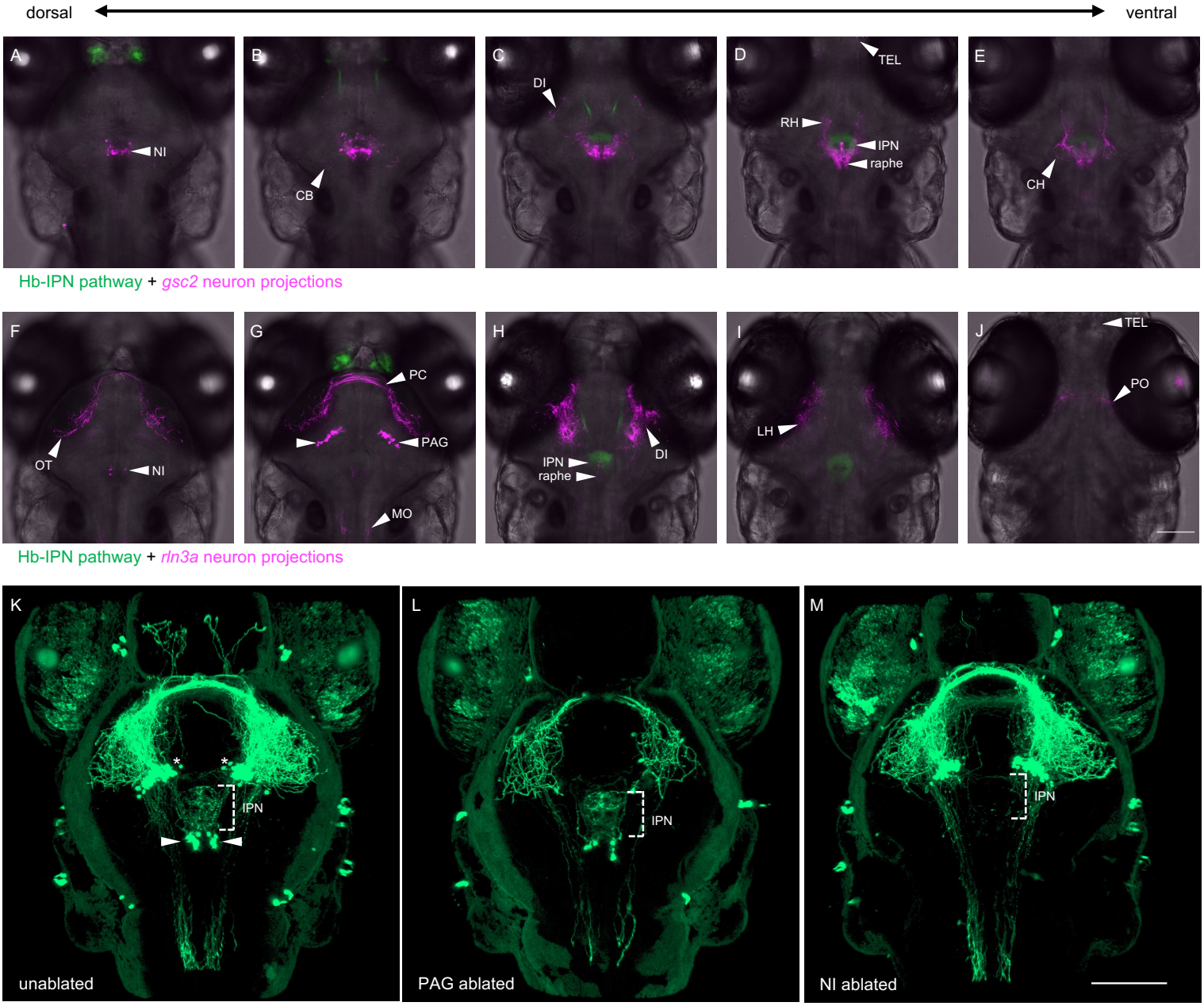
dorsal
ventral
A
NI
B
CB
C
DI
D
TEL
RH
IPN
raphe
E
CH
Hb-IPN pathway + gsc2 neuron projections
F
OT
NI
G
PC
PAG
MO
H
IPN
raphe
DI
I
LH
J
TEL
PO
Hb-IPN pathway + rln3a neuron projections
K
IPN
unablated
L
IPN
PAG ablated
M
IPN
NI ablated
rln3a neuron projections

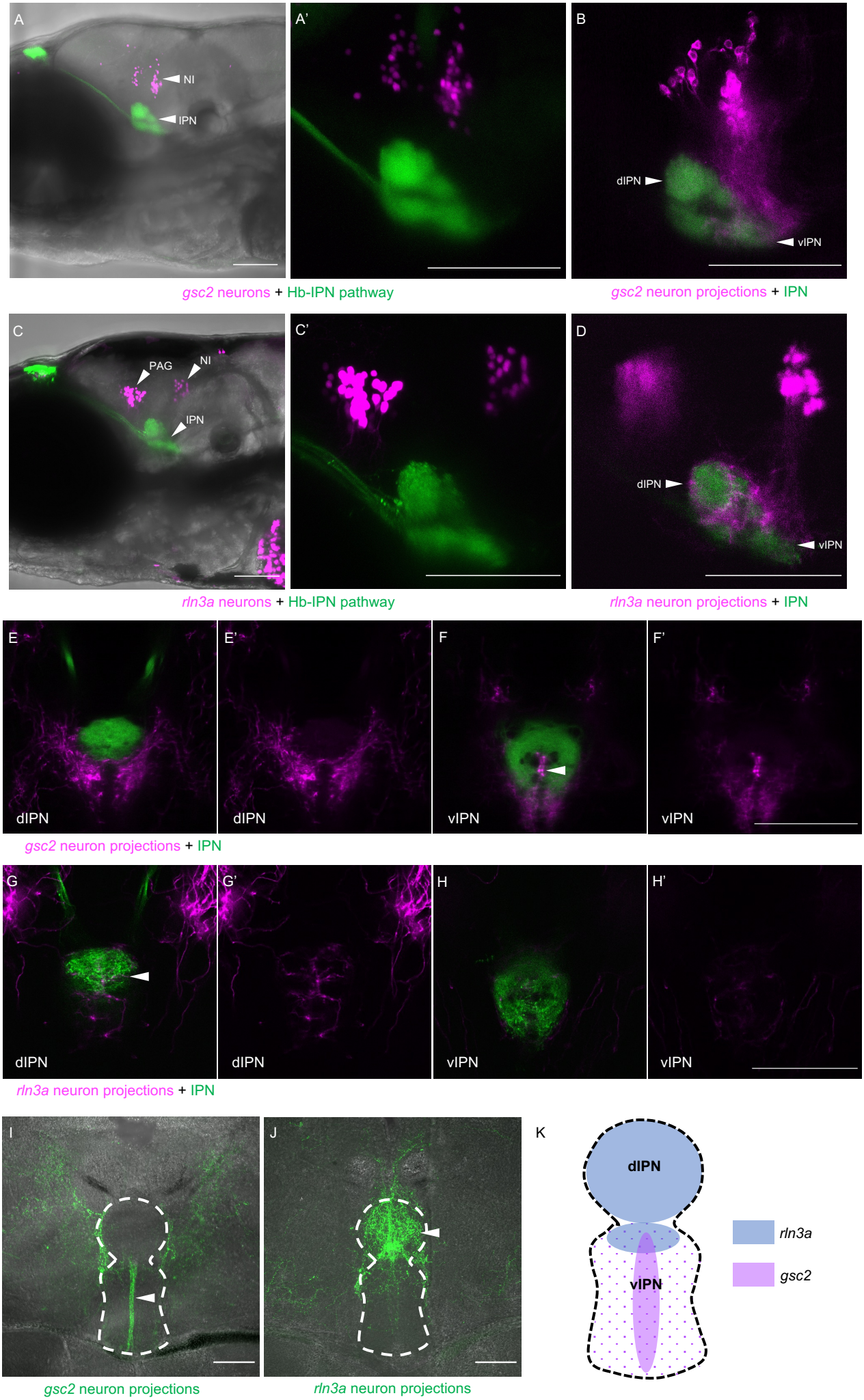
A
NI
IPN
A'
B
dIPN
vIPN
gsc2 neurons + Hb-IPN pathway
gsc2 neuron projections + IPN
C
PAG
NI
IPN
C'
D
dIPN
vIPN
rln3a neurons + Hb-IPN pathway
rln3a neuron projections + IPN
E
E'
F
F'
dIPN
dIPN
vIPN
vIPN
gsc2 neuron projections + IPN
G
G'
H
H'
dIPN
dIPN
vIPN
vIPN
rln3a neuron projections + IPN
I
J
K
dIPN
vIPN
rln3a
gsc2
gsc2 neuron projections
rln3a neuron projections

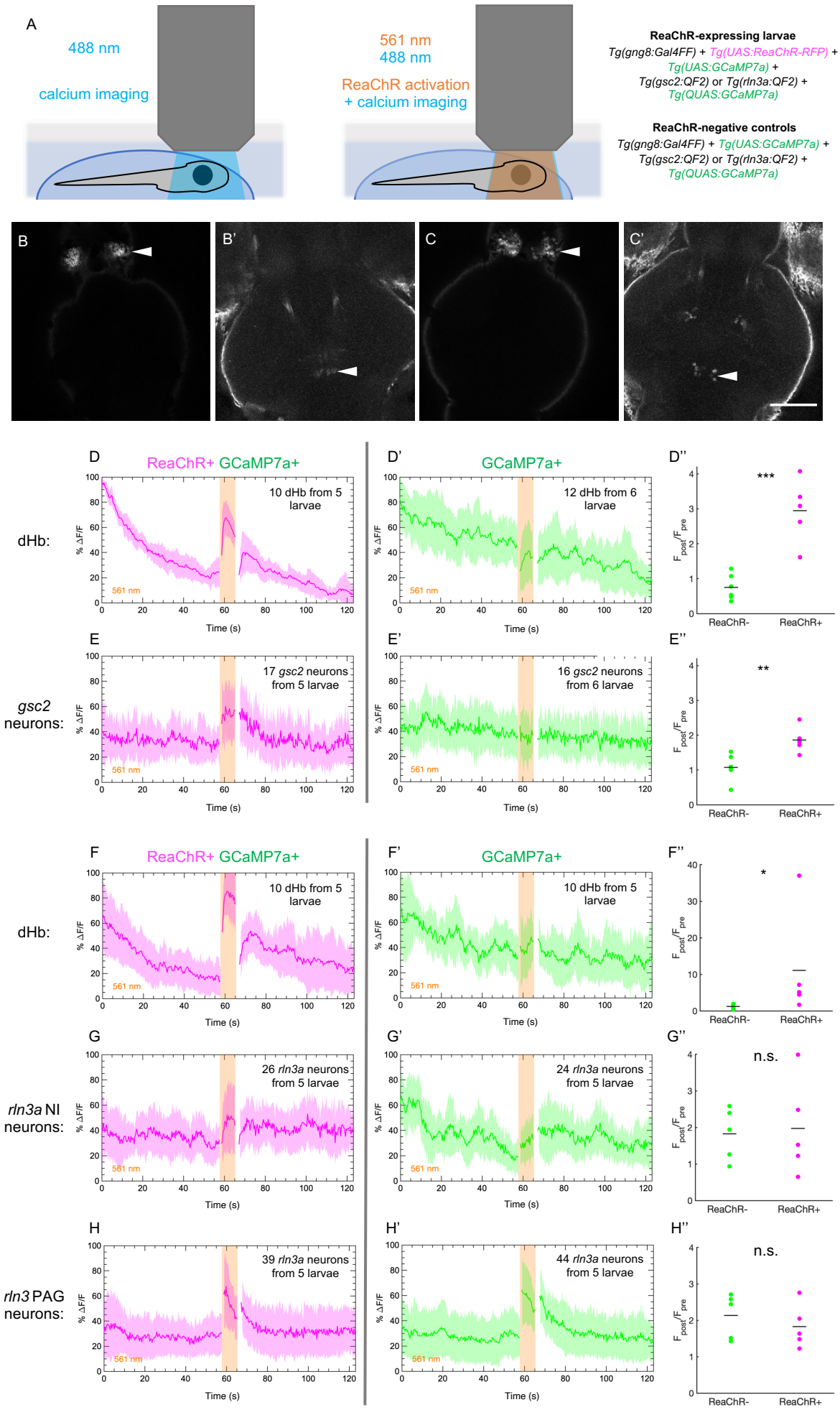
A
488 nm
calcium imaging
561 nm
488 nm
ReaChR activation
+ calcium imaging
ReaChR-expressing larvae
Tg(gng8:Gal4FF) + Tg(UAS:ReaChR-RFP) +
Tg(UAS:GCaMP7a) +
Tg(gsc2:QF2) or Tg(rln3a:QF2) +
Tg(QUAS:GCaMP7a)
ReaChR-negative controls
Tg(gng8:Gal4FF) + Tg(UAS:GCaMP7a) +
Tg(gsc2:QF2) or Tg(rln3a:QF2) +
Tg(QUAS:GCaMP7a)
B
B'
C
C'
D
ReaChR+ GCaMP7a+
10 dHb from 5 larvae
D'
GCaMP7a+
12 dHb from 6 larvae
D''
***
dHb:
E
17 gsc2 neurons from 5 larvae
E'
16 gsc2 neurons from 6 larvae
E''
**
gsc2 neurons:
F
ReaChR+ GCaMP7a+
10 dHb from 5 larvae
F'
GCaMP7a+
10 dHb from 5 larvae
F''
*
dHb:
G
26 rln3a neurons from 5 larvae
G'
24 rln3a neurons from 5 larvae
G''
n.s.
rln3a NI neurons:
H
39 rln3a neurons from 5 larvae
H'
44 rln3a neurons from 5 larvae
H''
n.s.
rln3 PAG neurons:
% ΔF/F
Time (s)
561 nm
F post/F pre
ReaChR-
ReaChR+

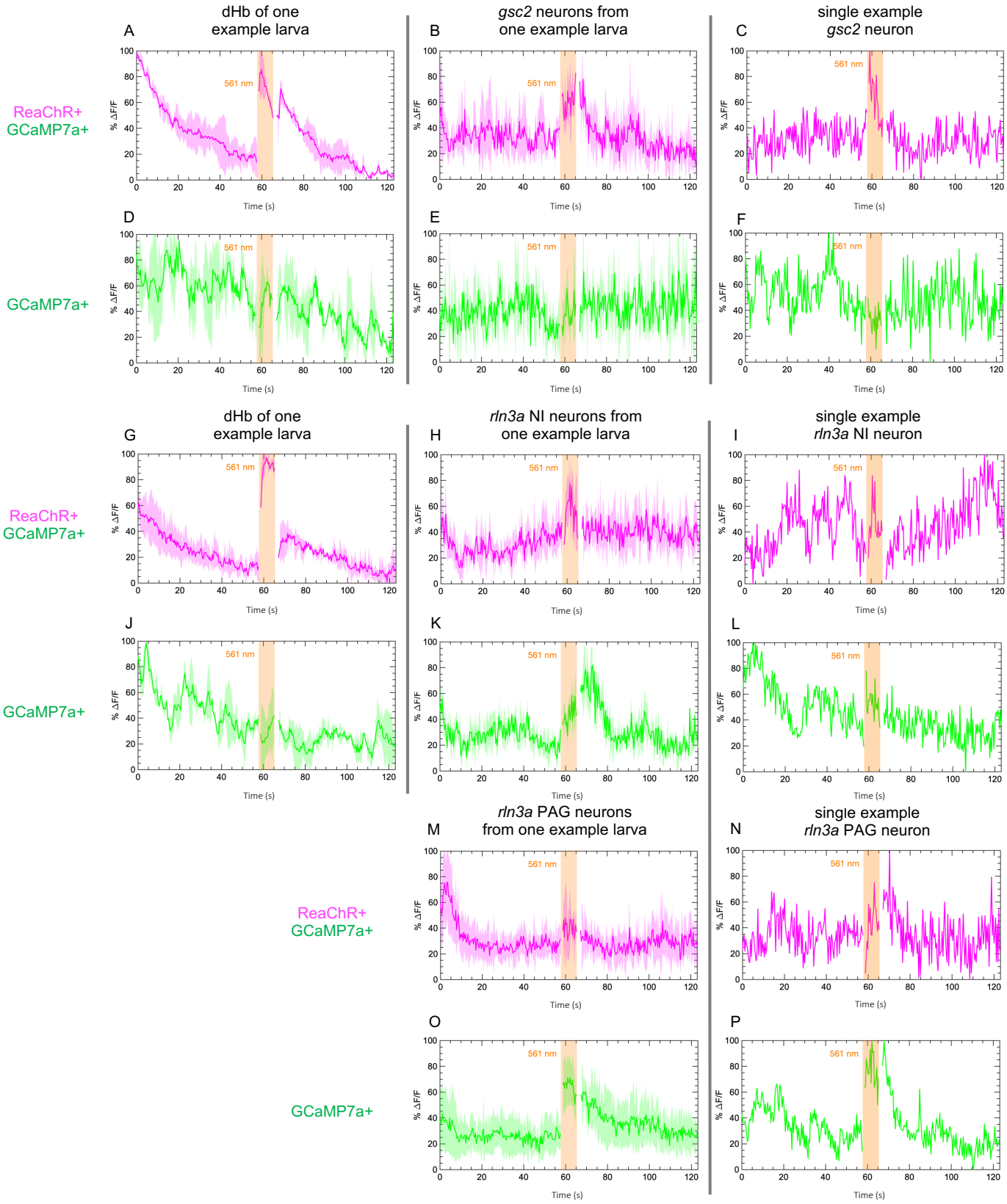
dHb of one example larva
gsc2 neurons from one example larva
single example gsc2 neuron
dHb of one example larva
rln3a NI neurons from one example larva
single example rln3a NI neuron
rln3a PAG neurons from one example larva
single example rln3a PAG neuron
ReaChR+ GCaMP7a+
GCaMP7a+
A
B
C
D
E
F
G
H
I
J
K
L
M
N
O
P
561 nm
% ΔF/F
Time (s)

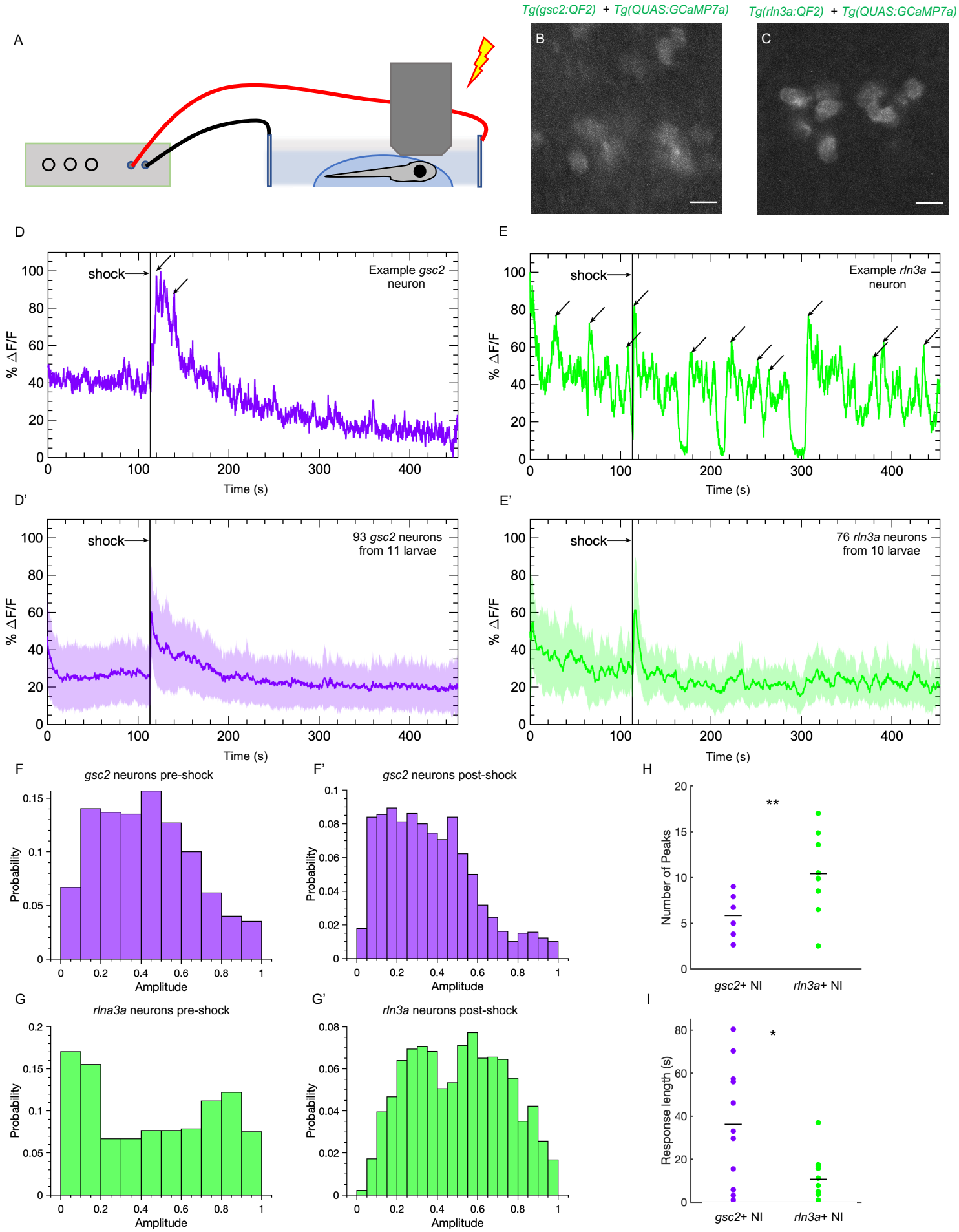
A
Tg(gsc2:QF2) + Tg(QUAS:GCaMP7a)
B
Tg(rln3a:QF2) + Tg(QUAS:GCaMP7a)
C
D
shock
Example gsc2 neuron
% ΔF/F
Time (s)
E
shock
Example rln3a neuron
% ΔF/F
Time (s)
D'
shock
93 gsc2 neurons from 11 larvae
% ΔF/F
Time (s)
E'
shock
76 rln3a neurons from 10 larvae
% ΔF/F
Time (s)
F
gsc2 neurons pre-shock
Probability
Amplitude
F'
gsc2 neurons post-shock
Probability
Amplitude
H
Number of Peaks
**
gsc2+ NI
rln3a+ NI
G
rlna3a neurons pre-shock
Probability
Amplitude
G'
rln3a neurons post-shock
Probability
Amplitude
I
Response length (s)
*
gsc2+ NI
rln3a+ NI

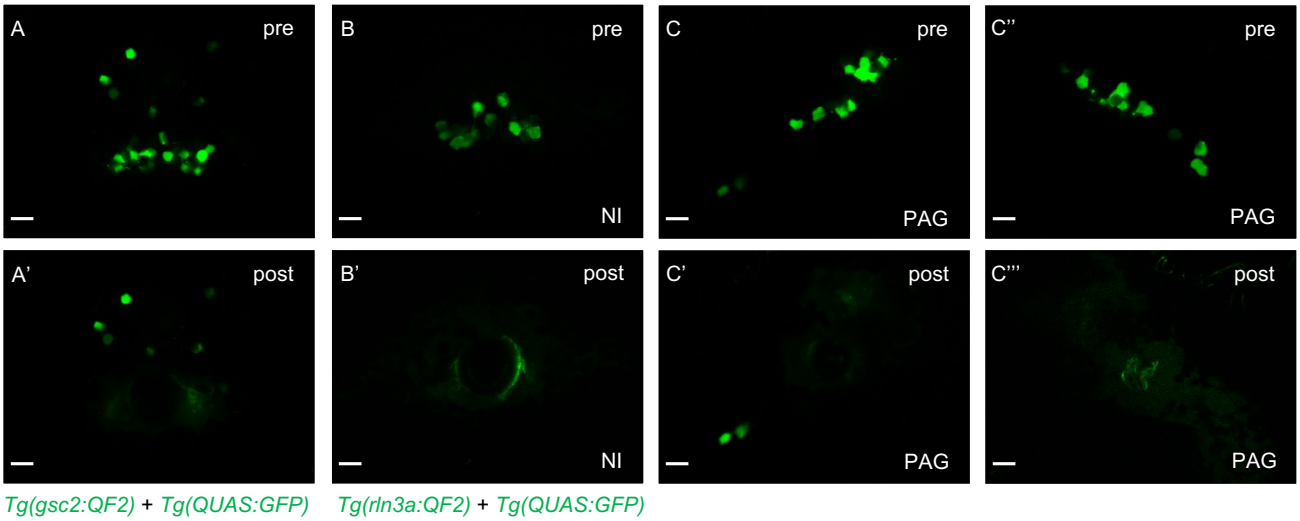
A
pre
B
pre
NI
C
pre
PAG
C''
pre
PAG
A'
post
B'
post
NI
C'
post
PAG
C'''
post
PAG
Tg(gsc2:QF2) + Tg(QUAS:GFP)
Tg(rln3a:QF2) + Tg(QUAS:GFP)

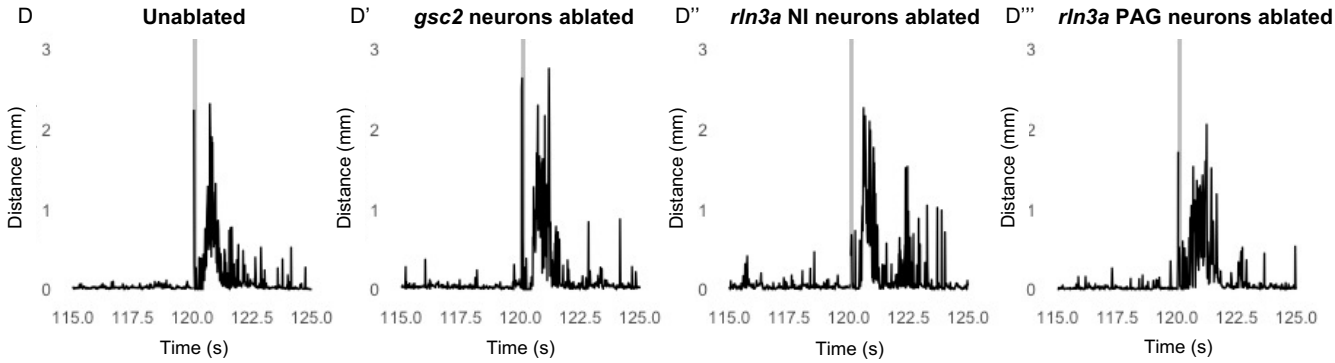
D
Unablated
D'
gsc2 neurons ablated
D''
rln3a NI neurons ablated
D'''
rln3a PAG neurons ablated
Distance (mm)
Time (s)
115.0
117.5
120.0
122.5
125.0

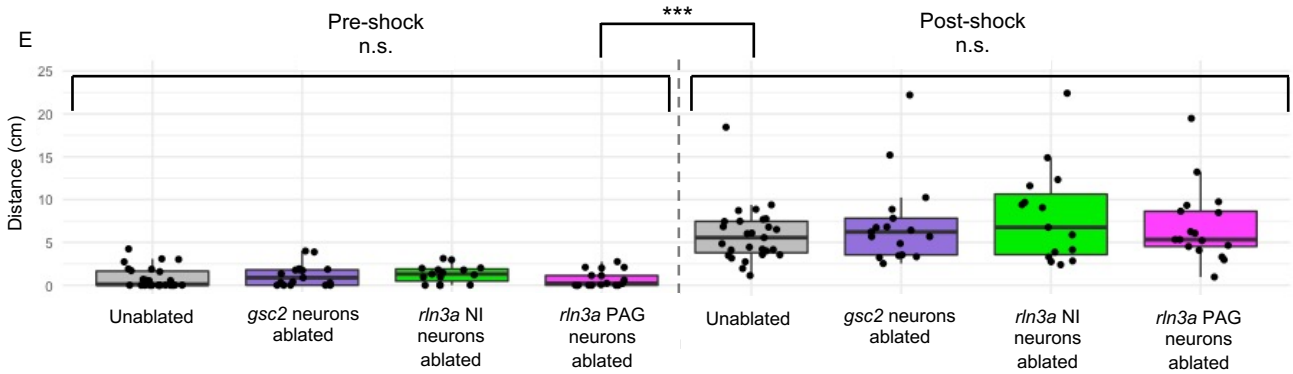
E
Pre-shock
n.s.
***
Post-shock
n.s.
Distance (cm)
Unablated
gsc2 neurons ablated
rln3a NI neurons ablated
rln3a PAG neurons ablated

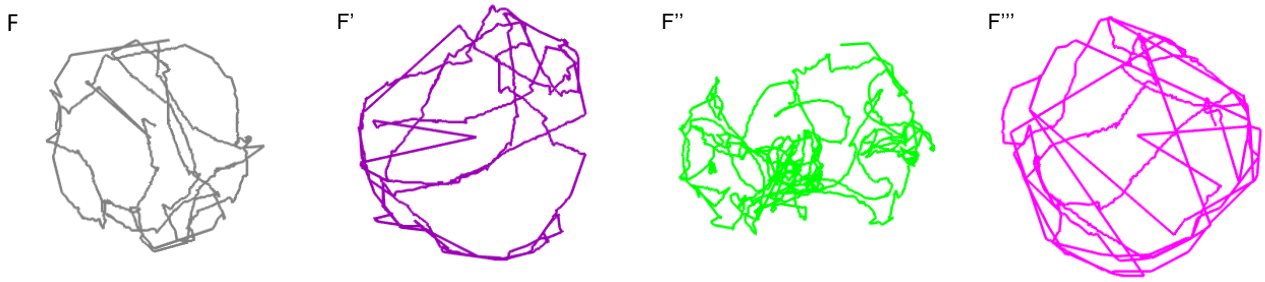
F
F'
F''
F'''

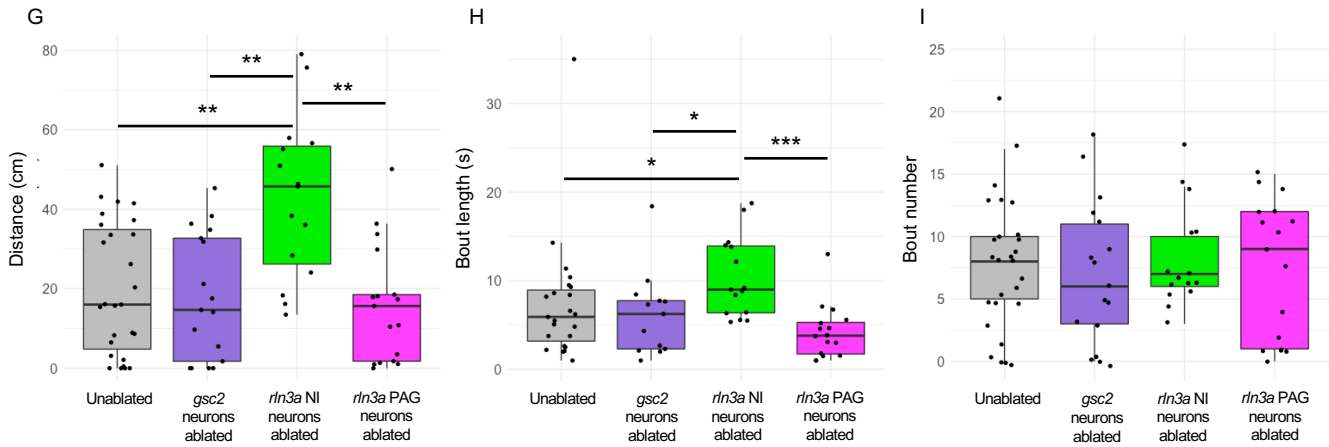
G
H
I
Distance (cm)
Bout length (s)
Bout number
Unablated
gsc2 neurons ablated
rln3a NI neurons ablated
rln3a PAG neurons ablated

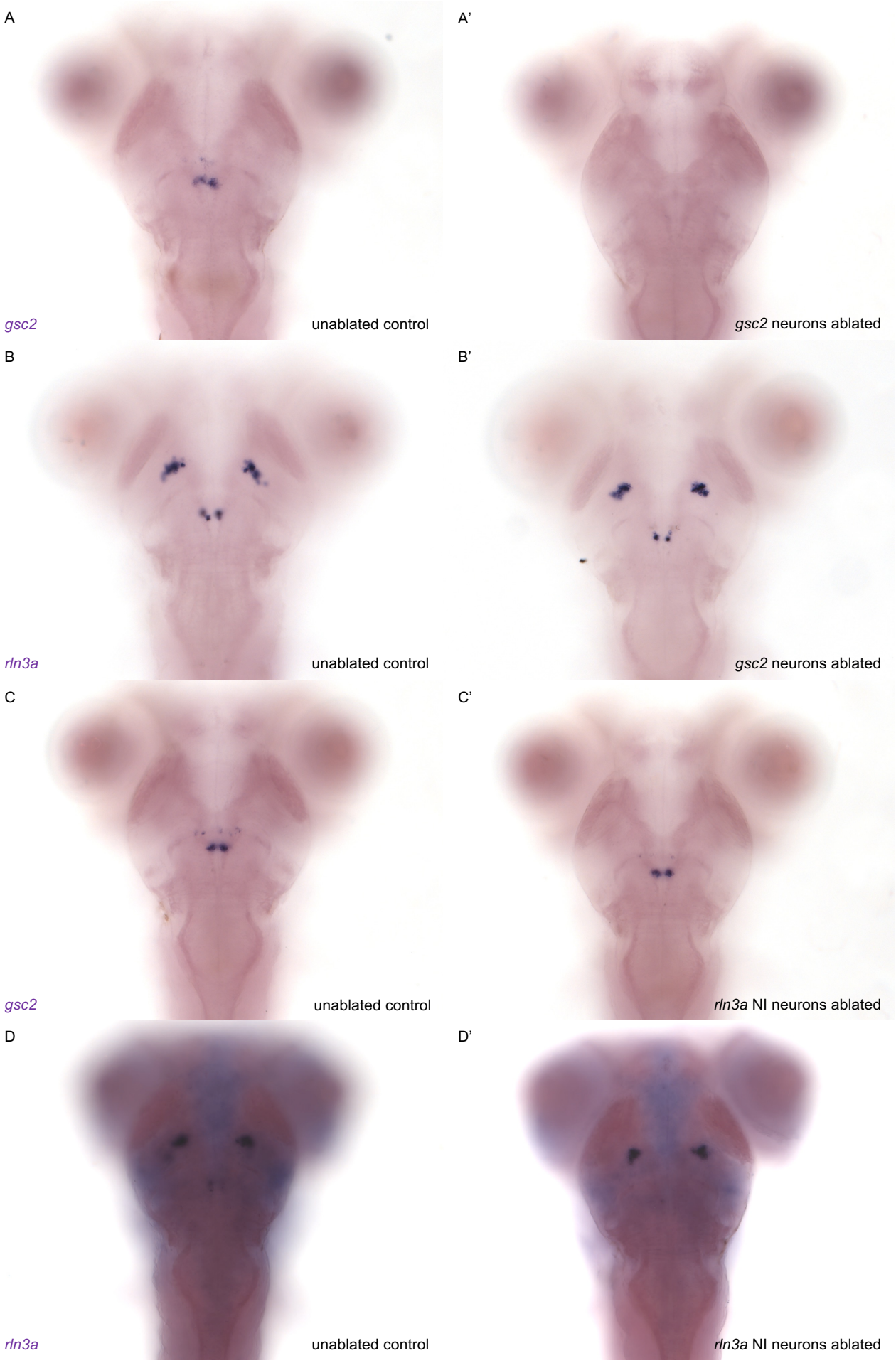
A
gsc2
unablated control
A'
gsc2 neurons ablated
B
rln3a
unablated control
B'
gsc2 neurons ablated
C
gsc2
unablated control
C'
rln3a NI neurons ablated
D
rln3a
unablated control
D'
rln3a NI neurons ablated

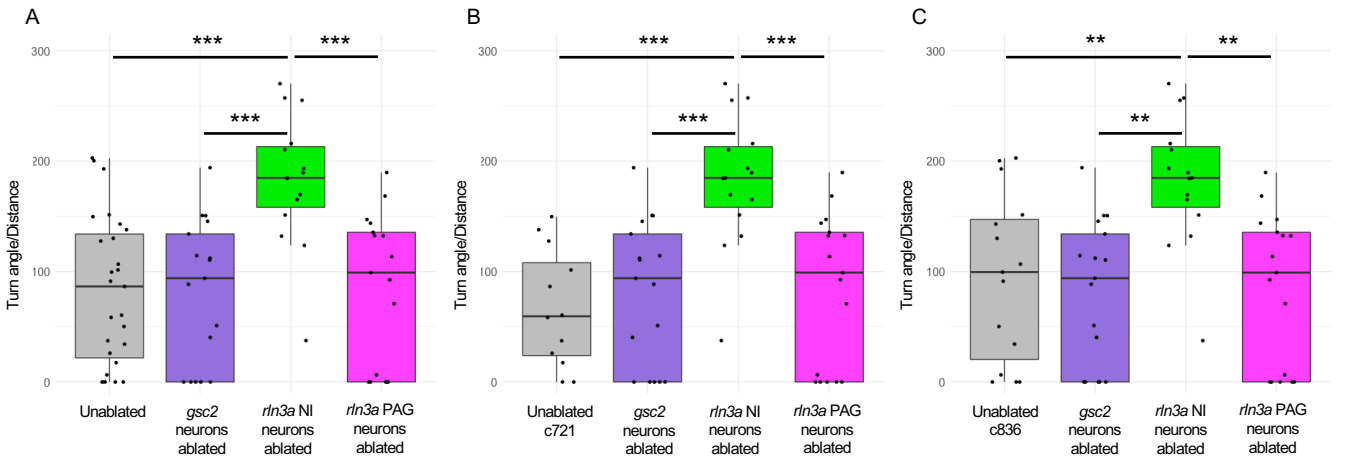
A
B
C
Turn angle/Distance
300
200
100
0
***
**
Unablated
Unablated c721
Unablated c836
gsc2 neurons ablated
rln3a NI neurons ablated
rln3a PAG neurons ablated

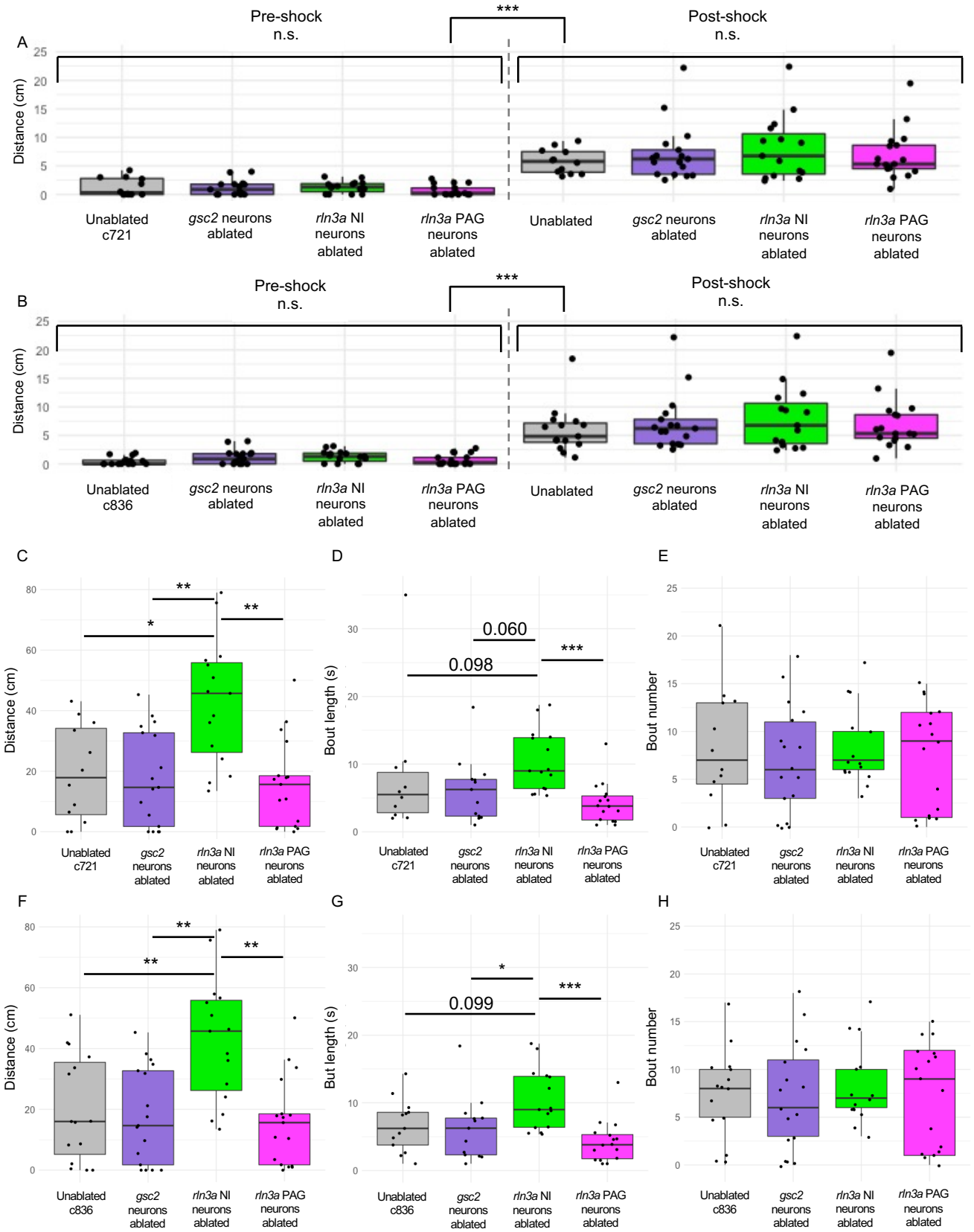
A
Pre-shock
n.s.
***
Post-shock
n.s.
Distance (cm)
Unablated c721
gsc2 neurons ablated
rln3a NI neurons ablated
rln3a PAG neurons ablated
Unablated
gsc2 neurons ablated
rln3a NI neurons ablated
rln3a PAG neurons ablated
B
Pre-shock
n.s.
***
Post-shock
n.s.
Distance (cm)
Unablated c836
gsc2 neurons ablated
rln3a NI neurons ablated
rln3a PAG neurons ablated
Unablated
gsc2 neurons ablated
rln3a NI neurons ablated
rln3a PAG neurons ablated
C
Distance (cm)
D
Bout length (s)
0.060
0.098
E
Bout number
F
Distance (cm)
G
But length (s)
0.099
H
Bout number